

This is a repository copy of *Decoupling ion energy and flux in intermediate pressure capacitively coupled plasmas via tailored voltage waveforms*.

White Rose Research Online URL for this paper:

<https://eprints.whiterose.ac.uk/177292/>

Version: Accepted Version

Article:

Doyle, Scott, Gibson, Andrew, Boswell, Rod et al. (2 more authors) (2020) Decoupling ion energy and flux in intermediate pressure capacitively coupled plasmas via tailored voltage waveforms. *Plasma Sources Science and Technology*. 124002. ISSN 0963-0252

<https://doi.org/10.1088/1361-6595/abc82f>

Reuse

This article is distributed under the terms of the Creative Commons Attribution-NonCommercial-NoDerivs (CC BY-NC-ND) licence. This licence only allows you to download this work and share it with others as long as you credit the authors, but you can't change the article in any way or use it commercially. More information and the full terms of the licence here: <https://creativecommons.org/licenses/>

Takedown

If you consider content in White Rose Research Online to be in breach of UK law, please notify us by emailing eprints@whiterose.ac.uk including the URL of the record and the reason for the withdrawal request.

Decoupling ion energy and flux in intermediate pressure capacitively coupled plasmas via tailored voltage waveforms

Scott J. Doyle^{1,2}, Andrew R. Gibson^{3,4}, Rod W. Boswell⁵, Christine Charles⁵, and James P. Dedrick²

¹Dept. of Atomic, Molecular and Nuclear Physics, University of Seville, Avda. Reina Mercedes, E-41012 Seville, Spain

²York Plasma Institute, Department of Physics, University of York, Heslington, York, YO10 5DD, UK

³Research Group for Biomedical Plasma Technology, Ruhr-Universität Bochum, Universitätsstraße 150, 44801 Bochum, Germany

⁴Institute of Electrical Engineering and Plasma Technology, Ruhr-Universität Bochum, Universitätsstraße 150, 44801 Bochum, Germany

⁵Space Plasma, Power and Propulsion Laboratory, Research School of Physics, The Australian National University, ACT 2601, Australia

¹E-mail: Scott.Doyle@Physics.org

October 12, 2020

Abstract

The discrete control of ion energy and flux is of increasing importance to industrially relevant plasma sources. The ion energy distribution functions (IEDFs) and net ion flux incident upon material surfaces in intermediate pressure (≈ 133 Pa, 1 Torr) radio-frequency capacitively coupled plasmas (rf CCPs) are coupled to the spatio-temporal sheath dynamics and resulting phase-averaged sheath potential. For single frequency driven discharges this co-dependence of ion energy and flux on the sheath potential limits the range of accessible operating regimes. In this work, experimentally benchmarked 2D fluid/Monte-Carlo simulations are employed to demonstrate quasi-independent control of the ion flux and IEDF incident upon plasma facing surfaces in a collisional (≈ 200 Pa, 1.5 Torr argon) rf hollow cathode discharge driven by multi-harmonic ($n \geq 2$) tailored voltage waveforms. The application of variable phase offset $n = 5$ tailored voltage waveforms affords a significant degree of control over the ion flux Γ_{Ar^+} and mean ion energy $\hat{\epsilon}_{Ar^+}$, modulating each by

factors of 2.9 and 1.6, respectively as compared to 1.8 and 1.6, achieved via $n = 2$ dual-frequency voltage waveforms. The disparate modulations achieved employing $n = 5$ tailored voltage waveforms demonstrate a significant degree of independent control over the mean ion energy and ion flux for collisional conditions, enabling access to a wider range of operational regimes. Maximising the extent to which ion energy and flux may be independently controlled enables improvements to plasma sources for technological applications such as plasma assisted material manufacture and spacecraft propulsion.

1 Introduction

Control of ion energy distribution functions (IEDFs) and particle fluxes incident upon plasma facing surfaces is of fundamental interest for the development of radio-frequency capacitively coupled plasma (rf-CCP) sources for industrial applications¹⁻⁴. Typically, the IEDF incident upon substrate surfaces plays a crucial role in the quality and homogeneity of etching and deposition processes, while the rate of these processes are primarily mediated by the ion flux⁵⁻⁷. In low-pressure plasma processing, control of the IEDF has traditionally been achieved through biasing the substrate, while the ion flux is mediated through varying the amplitude and frequency of the applied voltage waveform⁸⁻¹¹. However, these two techniques cannot be considered in isolation, as a dc biased substrate also influences the incident ion flux, and varying the applied voltage waveform modifies the ion energy distribution, limiting the range of available operating conditions^{12,13}.

Enhanced control of ion dynamics in rf-CCPs at low pressure ($\lesssim 67$ Pa, 0.5 Torr) has been achieved through the application of multi-frequency ‘tailored’ voltage waveforms¹⁴⁻²⁰. Tailored voltage waveforms comprise the superposition of two or more harmonics of a fundamental voltage frequency; by adjusting the relative phase or amplitude between harmonics, it is possible to introduce amplitude and slope asymmetries into the voltage waveform²¹⁻²⁴. Commonly employed tailored waveforms include ‘sawtooth’ waveforms^{25,26}, which exhibit a substantial slope asymmetry, and ‘peak’ or ‘valley’ waveforms²⁷⁻³⁰, which exhibit a substantial amplitude asymmetry, i.e. the maximum positive and negative applied voltages within one period of the fundamental applied frequency are not equal. These asymmetries directly influence the powered and grounded electrode sheath dynamics, leading to the formation of an electrical asymmetry effect (EAE). The EAE has been shown to modify existing physical^{25,30-32}, electron reflection³³ and secondary electron emission asymmetries^{34,35} present within the source.

The use of tailored voltage waveforms in low-pressure ($\lesssim 67$ Pa, 0.5 Torr) planar rf-CCP sources is already well established^{21,36-42}, where application of the EAE has enabled enhanced control of the ion energy while maintaining near-constant ion flux through a modulation of the dc self-bias voltage^{15,17,28,43}. Recently, work has begun to focus application in intermediate pressure discharges (≈ 133 Pa, 1 Torr)^{24,44,45}, atmospheric pressure discharges^{26,46-50}, and non-planar geometries^{32,41,51}. One such non-planar geometry involves the use of a powered hollow cathode (HC) through which gas is passed, the applications of which range from scalable arrays for homogeneous surface modification^{5,52} to micro-discharge sources for spacecraft propulsion⁵³⁻⁵⁵. The physically asymmetric geometry inherent to HC sources ensures that a substantial negative dc self-bias voltage forms adjacent to the powered electrode, required to balance the net positive and negative fluxes out of the plasma^{3,18,23}. As such, variation of the dc self-bias voltage in a HC source cannot typically be achieved without a

corresponding change in ion flux⁵¹. Similar behavior in the ion flux is observed when transitioning from low pressure discharges to intermediate pressure discharges^{26,32}.

In this work, we present experimentally validated 2D fluid-kinetic simulations of an intermediate pressure rf-CCP HC microdischarge source^{56–59} employing dual-frequency and multi-harmonic tailored voltage waveforms to achieve discrete control of ion energy and flux. Descriptions of the experimental setup and numerical model are given in sections 2.3 and 2.2, respectively, and an overview of the tailored voltage waveforms employed are presented in section 2.1. Prior to assessing the effects of each type of tailored voltage waveform on the ion dynamics, an experimental comparison is first performed in section 3 to benchmark the numerical approach. Following this, the degree of control afforded over the ionisation mechanisms, sheath dynamics, and resulting ion densities and fluxes are presented in section 4. Finally, the degree of control afforded over the ion energy distribution functions (IEDFs) is examined in section 5, and the prospect of quasi-independent control over the ion flux and ion energy is demonstrated in 5.1.

2 Experimental and Numerical Methodologies

2.1 Tailored Voltage Waveforms

The tailored voltage waveforms employed in this investigation comprise $n = 2$ dual-frequency voltage waveforms and $n = 5$, tailored voltage waveforms¹⁹, where n denotes the number of harmonic components. Both types of voltage waveforms are constructed exclusively from harmonics of a 13.56 MHz fundamental frequency, as described by equation 1.

$$\phi_{\text{rf}}(t) = \sum_{k=1}^n \phi_k \sin(k\omega_0 t + \theta_k) \quad (1)$$

Here, $\phi_{\text{rf}}(t)$ is the time dependent voltage of the combined waveform, ϕ_k is the amplitude of the k 'th harmonic component, $\omega_0 = 2\pi f_0$ is the fundamental angular frequency, θ_k is the phase offset of harmonic k and n is the total number of applied harmonics. The amplitude of each harmonic component ϕ_k is determined in one of two ways; either by sharing the amplitude equally across all harmonics, via equation 2, which is employed to produce both 'traditional' $n = 5$ tailored voltage waveforms and $n = 2$ dual-frequency voltage waveforms¹⁴.

$$\phi_k = \frac{\phi_0}{n} \quad (2)$$

Or by linearly reducing the amplitude contribution of the higher harmonic components, via equa-

tion 3 (adapted from Ref. 15), producing ‘optimised’ $n = 5$ tailored voltage waveforms, which minimize the voltage amplitude oscillation between successive peaks.

$$\phi_k = \phi_0 \frac{n - k + 1}{(1 + n)^2} \quad (3)$$

Optimised $n = 5$ tailored voltage waveforms are utilized to match experimental conditions in section 3. All other results presented in sections 4 and 5 employ voltage waveforms with harmonic component amplitudes as calculated by equation 2, enabling a more direct comparison between the $n = 2$ dual-frequency and $n = 5$ tailored voltage waveform shapes. When considering such $n = 2$, $k = 1, 2$ dual-frequency voltage waveforms, equation 1 simplifies to:

$$\phi_{\text{rf}}(t) = \frac{\phi_0}{2} \sin(k\omega_0 t + \theta_1) + \frac{\phi_0}{2} \sin(2k\omega_0 t + \theta_2) \quad (4)$$

Note that for dual-frequency voltage waveforms, only the upper harmonic phase offset is varied such that $\theta_1 = 0^\circ$ and $\theta_2 = \theta$ in equation 4. This distinction has the effect of reversing the ‘parity’, of the dual-frequency waveforms relative to the tailored voltage waveforms, see figure 1 (c), but has no effect on the amplitudes. The $n = 5$ tailored waveforms generated from equation 1 employ a homogeneous phase offset for all harmonic phase-offsets such that $\theta = \theta_n \forall n$. Tailored waveforms exhibiting the largest amplitude asymmetries are obtained for $\theta = 90^\circ$, henceforth denoted as a ‘peak’ waveform²⁹, and $\theta = 270^\circ$, denoted as a ‘valley’ waveform²⁸. Phase offsets between these two extrema produce intermediate tailored voltage waveforms, with shapes smoothly varying between the peak and valley waveforms.

Examples of $n = 2$, $k = 1, 2$ dual-frequency and $n = 5$, tailored voltage waveforms generated employing equations 1 and 4 are shown in figures 1 (a) and (b), respectively.

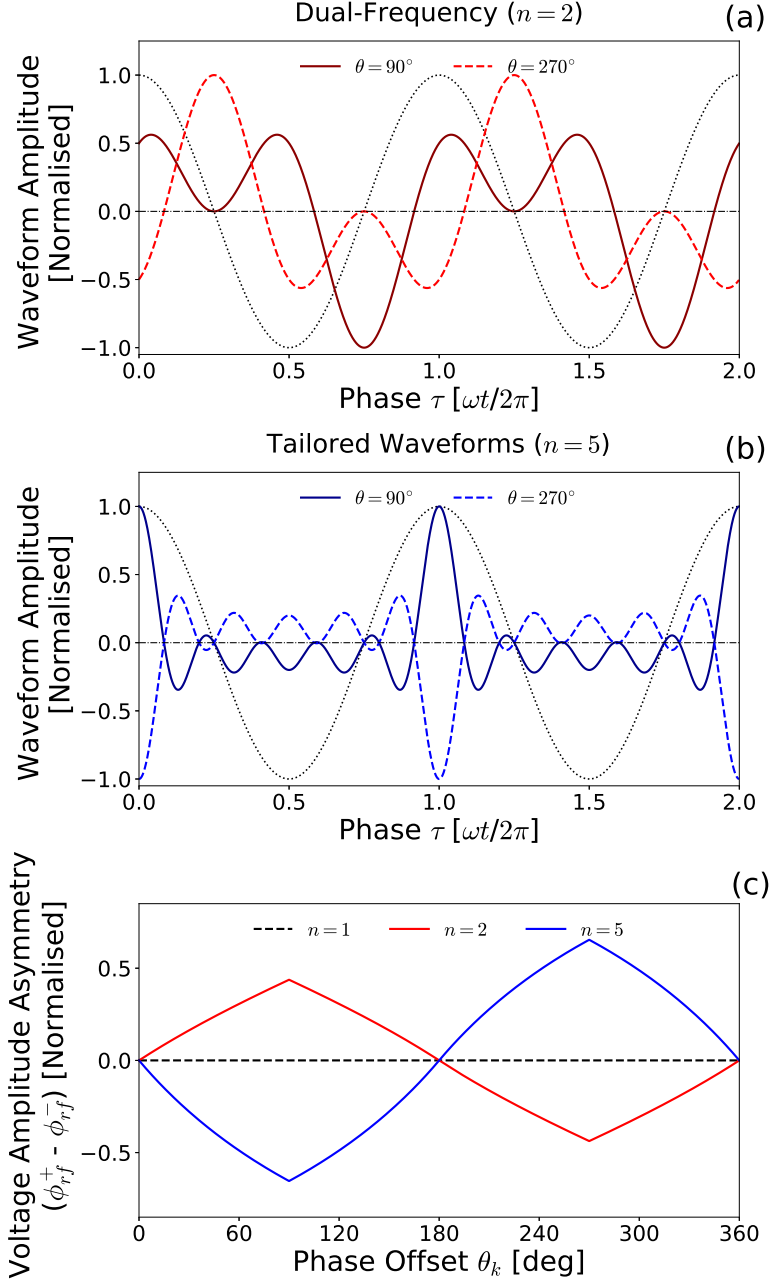


Figure 1: Normalised (a) $n = 2$ dual-frequency and (b) $n = 5$ tailored voltage waveforms employing phase offsets of $\theta = 90^\circ$ and $\theta = 270^\circ$, and (c) the resulting voltage amplitude asymmetries $(\phi_{rf}^+ - \phi_{rf}^-)$ for both waveforms with respect to phase offsets in the range $0^\circ \leq \theta \leq 360^\circ$. Waveform harmonic components are computed employing equation 2. Sinusoidal waveforms employing the fundamental frequency (13.56 MHz) are presented in (a) and (b) by the dotted lines for comparison.

Examining the dual-frequency waveforms in figure 1 (a), it can be seen that varying the upper harmonic phase offset θ alters the maximum positive ϕ_{rf}^+ and minimum negative ϕ_{rf}^- waveform amplitudes, while maintaining a net zero time-averaged voltage. For the two dual-frequency voltage waveforms presented, the maximum positive normalised amplitude varies from $\phi_{rf}^+ = 0.5$ to $\phi_{rf}^+ = 1.0$ for $\theta = 90^\circ$ and $\theta = 270^\circ$, respectively and visa-versa with respect to the minimum negative amplitude. This effect is more pronounced for the $n = 5$ tailored voltage waveforms, shown in figure 1 (b), where peak ($\theta = 90^\circ$) and valley ($\theta = 270^\circ$) waveforms exhibit exhibit normalised amplitude ranges

of ϕ_{rf}^+ , $\phi_{rf}^- = +1.0, -0.25$, to ϕ_{rf}^+ , $\phi_{rf}^- = +0.25, -1.0$, respectively. In describing this behaviour, it is useful to define the voltage amplitude asymmetry ($\phi_{rf}^+ - \phi_{rf}^-$) as the maximum difference between the positive and negative amplitude within a single rf cycle.

The voltage amplitude asymmetries for $n = 2$ and $n = 5$ tailored voltage waveforms employing phase offsets in the range $0^\circ \leq \theta \leq 360^\circ$, are shown in figure 1 (c). The greatest degree of modulation is achieved for $n = 5$ tailored voltage waveforms, achieving a maximum 65% modulation within a single rf phase cycle, as compared to only a maximum of only 44% for dual-frequency voltage waveforms. Further, $n = 5$ tailored voltage waveforms exhibit a steeper change in voltage amplitude asymmetry around $\theta = 180^\circ$, while dual-frequency voltage waveforms exhibit a near-linear modulation between their maximum and minimum values. Note also the reversal in parity between the $n = 2$ dual-frequency waveforms and the $n = 5$ tailored waveforms, as discussed with respect to equation 4.

The ‘magnitude’ of the EAE applied to the plasma varies in proportion to the voltage amplitude asymmetry and to the plasma response to the applied rf voltage waveform. The magnitude of the EAE is typically quantified through the symmetry parameter²² ϵ_s , computed as shown in equation 5.

$$\epsilon_s = \frac{\hat{n}_{Sp}}{\hat{n}_{Sg}} \left(\frac{Q_{Sg}}{Q_{Sp}} \right)^2 \left(\frac{A_p}{A_g} \right)^2 \frac{I_{Sg}}{I_{Sp}} = \left| \frac{\phi_{Sg}}{\phi_{Sp}} \right| \quad (5)$$

Here, \hat{n}_{Sp} , \hat{n}_{Sg} are the sheath averaged ion densities, Q_{Sg} , Q_{Sp} are the maximum electrode surface charges, A_p , A_g represent electrode surface areas and ϕ_{Sg} , ϕ_{Sp} are the maximum voltage drops across each respective sheath, where subscripts p and g denote the powered and grounded electrodes, respectively. It is perhaps useful to note here that as the HC geometry exhibits an axially aligned geometric asymmetry (i.e. varying along the source axis), the interpretation of these variables depends upon the choice of axial location. The parameters I_{Sp} and I_{Sg} , denoted the sheath integrals, represent the distribution of charge within each sheath and are defined as:

$$I_{Sx} = 2 \int_0^1 \frac{n_i(R)}{\hat{n}_{Sx}} \xi \, d\xi \quad \text{where} \quad \xi = \frac{R}{S_x} \quad (6)$$

where S_x is the maximum sheath extension from the x ’th plasma facing surface. The dc self-bias voltage η_{dc} resulting from an EAE of magnitude ϵ_s can then be readily calculated through an application of Kirchhoff’s law⁶⁰. If the change in voltage across the plasma bulk is small relative to the sheath potential³, as is the case in this work where $\Delta\phi_{fp}/\Delta\phi_S \leq 10\%$, one can obtain an expression for the dc self-bias voltage as shown in equation 7:

$$\eta_{dc} = - \frac{\phi_{rf}^+ + \epsilon_s \phi_{rf}^-}{1 + \epsilon_s} \quad (7)$$

Here, ϕ_{rf}^+ and ϕ_{rf}^- are the extrema in the applied tailored voltage waveform amplitudes with a single rf period, as before. The dc self-bias voltage is set negative, such is the case of a typical hollow cathode source where the grounded electrode area exceeds the powered electrode area³. Notably, the degree of control afforded over the dc self-bias voltage relies upon two factors: 1) the extent to which the positive and negative voltage waveform amplitudes can be modulated, analytically computed in figure 1; and 2) the extent to which the phase-resolved sheath potentials can be modulated via ϵ_s , requiring a consideration of the plasma response to the applied voltage waveforms and necessitating a numerical approach.

2.2 Description of the Simulation Model

Two-dimensional fluid-kinetic simulations were undertaken using the Hybrid Plasma Equipment Model (HPEM)⁶¹ to examine the phase-resolved sheath and phase-averaged ion dynamics. A full description of the mesh and numerical methods applied can be found in Ref. 59, a summary is provided here. The simulated region is shown in figure 2 by the shaded grey area. The simulation mesh consisted of a rectilinear grid of 64×152 ($R \times Z$) cells in a cylindrically symmetric geometry, corresponding to a radial resolution of 0.125 mm per cell and an axial resolution of 0.5 mm per cell. A higher radial resolution was employed to adequately resolve the sheath dynamics, and associated ion behaviour, perpendicular to the alumina surface adjacent to the powered electrode. The sheath extension is calculated as in Ref. 51, where the radial sheath edge S_R is determined as the radius R that satisfies the Brinkmann criterion⁶².

The model employs a fluid treatment of background, thermalised, species and a kinetic treatment of non-thermal species. The energy distribution functions of all heavy particle species are assumed to be Maxwellian, while the distribution function of fluid electrons are determined by a two-term approximation of the Boltzmann equation. The species considered within the fluid model are: Ar, Ar(4s), Ar(4p), Ar(4d), Ar₂^{*}, Ar⁺, Ar₂⁺ and e⁻, where the reaction mechanism is as discussed in Ref. 63. Gas-phase electron-neutral and electron-ion collisions include elastic, excitation and ionisation reactions as presented in Ref. 63. Cascade processes, multi-step ionisation and heavy particle mixing between excited species are also included, the interaction rate coefficients for which are obtained from Refs. 64–68. Ion-neutral charge exchange collisions are employed with a rate coefficient of $5.66 \times 10^{-10} \text{ cm}^3 \text{ s}^{-1} (T_g/300)^{0.5}$ where T_g is the neutral-gas temperature⁶⁹.

Secondary electron emission is accounted for through an energy-independent model, where secondary electron flux is proportional to the incident ion flux and secondary electron emission coefficient. This coefficient is set to $\gamma = 0.2$ for the alumina wall, and $\gamma = 0.0$ for all other surfaces⁷⁰. The

behaviour of secondary electrons released from the alumina surface following ion bombardment and ion energy distributions for Ar^+ incident on the radial wall at $R, Z = 2.1, 21$ mm are obtained via a kinetic Monte-Carlo algorithm employing the same reaction mechanism as used in the gas phase⁶¹. The effects of secondary electrons are updated at each simulation iteration, while Ar^+ ion energy distribution functions are obtained using a Monte-Carlo algorithm only on the final iteration, following simulation convergence.

2.3 Description of the Experimental Setup

The rf-CCP HC microdischarge source, shown in figure 2, employs a copper annular powered electrode positioned around an 18 mm long alumina tube through which gas is passed⁵⁶. The source is mounted to, and electrically isolated from, an expansion chamber by a 300 mm long Pyrex glass tube. A base pressure of 1.33 Pa (0.01 Torr) is achieved via a scroll pump (not shown) in combination with a pressure gauge mounted to the plenum. Argon gas, at a flow rate of 100 sccm ($1.786 \text{ mg min}^{-1}$), is introduced through the plenum at the upstream side of the source, resulting in an upstream pressure of between 186 - 226 Pa (1.4 - 1.7 Torr), via variable neutral gas heating within the source, and a downstream expansion chamber pressure of 113 Pa (0.85 Torr). A Pyrex glass window located at the upstream end of the plenum enables optical access along the axial length of the source.

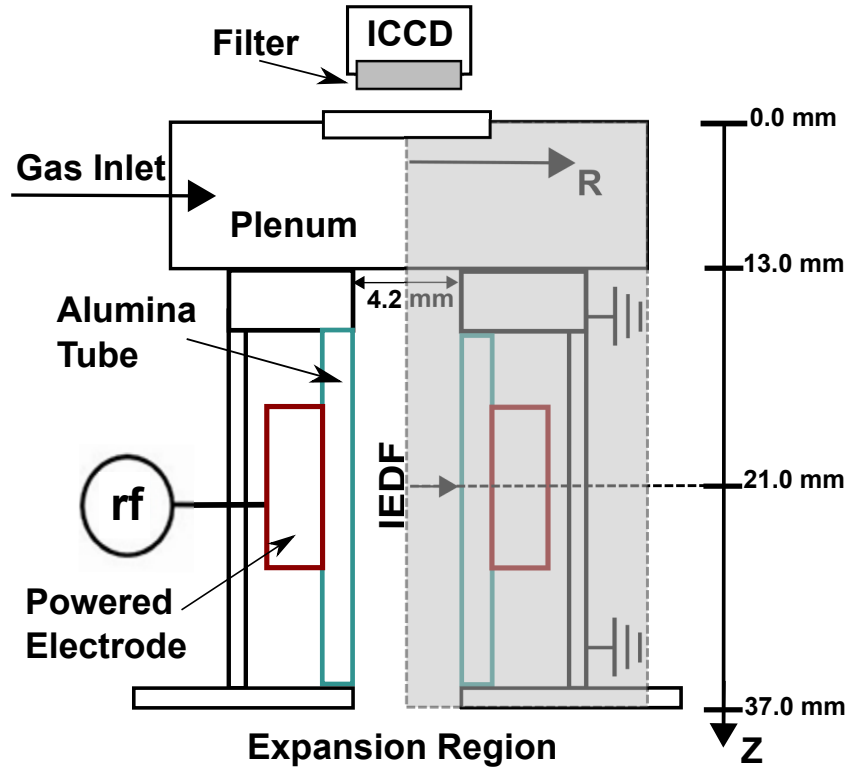


Figure 2: Schematic of the experimental setup (not to scale), where the simulated region is denoted by the shaded gray area. The imaging plane of the ICCD camera is centered on the midplane of the powered electrode, denoted by the dashed line ($Z = 21$ mm). Simulated IEDFs are obtained from Ar^+ ions incident on the radial wall at $R, Z = 2.1, 21$ mm as denoted by the solid blue arrow. The electrical circuit and tailored voltage feedback mechanism is shown in more detail in figure 3. Figure adapted from Ref. 59.

Power is supplied via an arbitrary waveform generator (Keysight 33621A, 120 MHz) and broadband amplifier (Prana GN500D, 0.01 - 220 MHz) connected in series with the powered electrode (see figure 3, no separate matching network is employed within this work, with reflected power being dissipated within the amplifier. As the grounded electrode area in contact with the plasma exceeds the powered electrode area, a dc self-bias voltage forms on the surface of the alumina wall adjacent to the powered electrode to maintain current continuity^{3,71}. Argon ions are accelerated through the dc self-bias enhanced sheath potential and undergo ion-neutral charge exchange collisions, resulting in significant neutral gas heating localised within the powered electrode sheath^{57,72,73} where maximum on-axis neutral gas temperatures typically vary between 600 – 1100 K^{13,59}. Secondary electrons, released through positive ion bombardment, are accelerated back into the plasma bulk at high, non-thermal energies (above 50 eV), representing an efficient additional ionisation mechanism^{74,75}.

The applied voltage waveforms are maintained and measured employing a SOLAYL SAS Vigilant Power Monitor (VPM), placed in series with the source via a 50 Ω coaxial cable and a vacuum feedthrough, in conjunction with a feedback-control loop shown in figure 3.

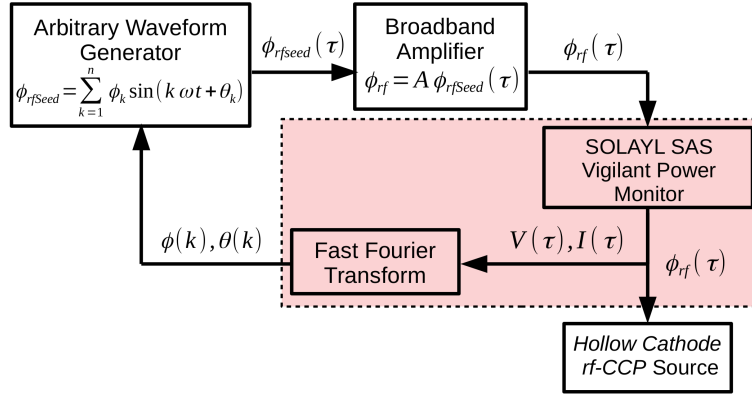


Figure 3: Schematic of the tailored voltage waveform feedback mechanism, sections employing the SOLAYL SAS Vigilant Power Monitor or associated software are highlighted in red.

The desired tailored voltage waveform shape are first specified manually within the VPM through selecting the appropriate harmonic amplitudes $\phi(k)$ and phase offsets $\theta(k)$, the mathematics of which are as discussed previously in section 2.1. The corresponding harmonic components are superimposed within the arbitrary waveform generator, creating a tailored seed waveform ϕ_{rfSeed} , where typically $\phi_{rfSeed} \leq 1$ V, which is then amplified by a factor A prior to being coupled to the powered electrode. Deformations arising during amplification and from impedance mismatches are reduced through the VPM actively modifying the input $\phi(k)$ and $\theta(k)$ to the arbitrary waveform generator such that the measured $\phi(k)$ and $\theta(k)$ converge towards the desired waveform shape. This feedback mechanism enables the generation of tailored voltage waveforms within $\approx 5\%$ of the target amplitude and tem-

poral shape. During measurements the feedback system was disabled to ensure a non-varying voltage waveform shape.

Phase-resolved optical emission spectroscopy (PROES)^{76,77} was performed to enable a comparison of the measured and simulated electron excitation rates, and hence also the phase-resolved sheath dynamics. Previous work has demonstrated agreement between the measured and simulated phase-resolved, $\text{Ar}(2p_1)$ electron impact excitation rates in this source for single frequencies up to 40.68 MHz^{13,59} and for dual-frequency operation⁵¹. Images were acquired with an ICCD camera (Andor iStar DH344T-18U-73, 1024×1024 array, pixel size: $13 \times 13 \mu\text{m}^2$) employing an optical gate width of 1.7 ns and a 750.466 nm bandpass filter (LOT-QuantumDesign, 1 nm FWHM). A depth of field of 24 mm, corresponding to the axial length of the source region, was applied to the simulated PROES images through a top hat integration along the line of sight⁷⁸.

3 Electron Dynamics: Measurements and Simulations

Agreement between measured and simulated phase-resolved $\text{Ar}(2p_1)$ excitation structures in this source has previously been achieved for varying single frequency operation in Ref. 13 and both odd-even ($k = 1, 2$) and odd-odd ($k = 1, 3$) dual-frequency $n = 2$ waveforms in Ref. 51. This section extends this agreement to $n = 5$ tailored voltage waveforms through a similar spatio-temporal excitation structure analysis.

Figure 4 shows the measured and simulated phase-resolved $\text{Ar}(2p_1)$ excitation rates for varying applied voltage waveform shape for a $\phi_0 = 240 \text{ V}$, $\approx 200 \text{ Pa}$ (1.5 Torr) argon discharge. Measured $\text{Ar}(2p_1)$ excitation rates for operation employing a single 13.56 MHz sinusoidal waveform, an optimised $n = 5$, $\theta = 90^\circ$ peak waveform and an optimised $n = 5$, $\theta = 270^\circ$ valley waveform are shown in figures 4 (a-c), respectively, while the associated simulated excitation rates are shown in figures 4 (d-f). The measured and simulated phase-resolved electrode potentials ϕ_{rf} and simulated dielectric potentials ϕ_{dc} are shown in figures 4 (g-i), where the phase-averaged dc self-bias voltages η_{dc} , equivalent to equation 7, are denoted by the dashed red lines. Both peak and valley waveforms employ harmonic components as computed by equation 3, i.e. the so-called optimised peak and valley waveforms.

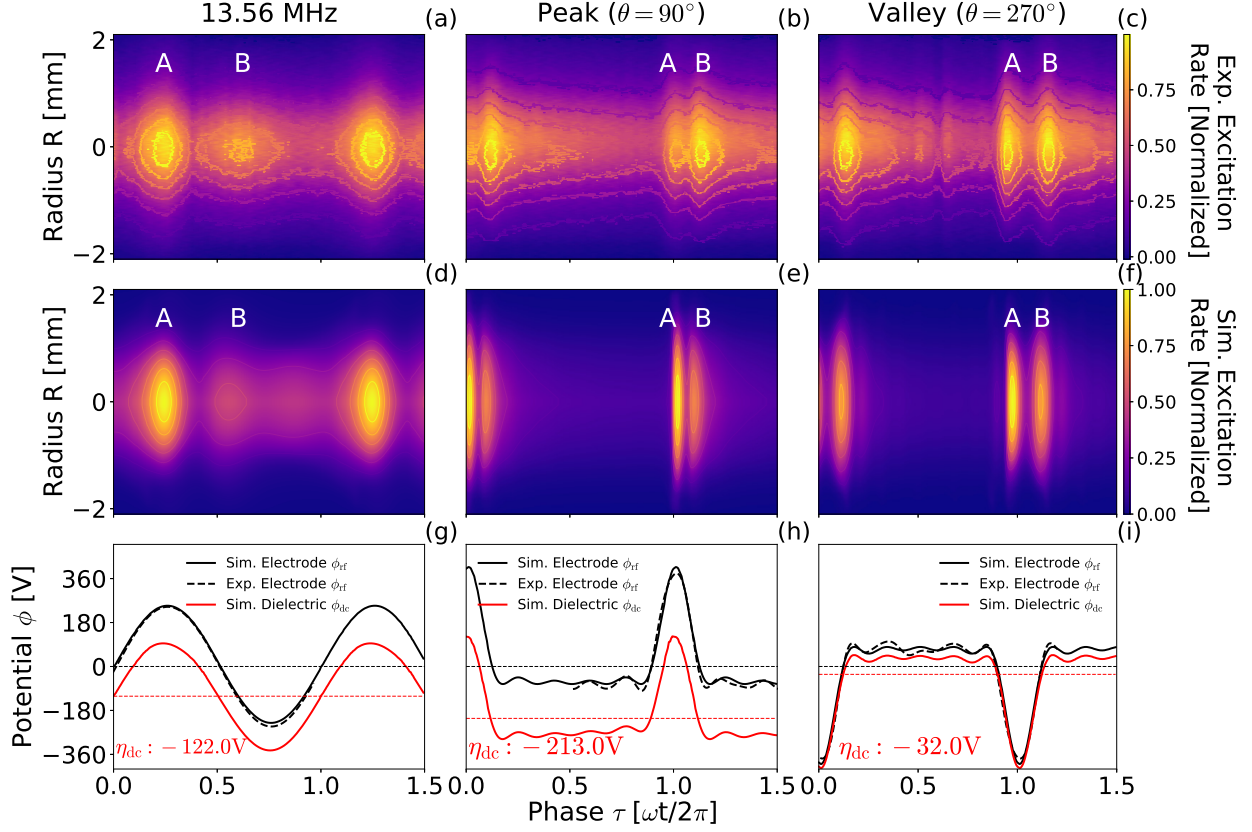


Figure 4: Phase resolved $\text{Ar}(2p_1)$ excitation rates for single-frequency sinusoidal and $n = 5$ optimised peak and valley tailored voltage waveforms, where harmonic components are computed employing equation 3. Experimental measurements are shown in panels (a)-(c), simulations in (d)-(f) and the corresponding applied voltage and dielectric surface potential waveforms in (g)-(i), respectively. In (g)-(i), measured and simulated applied voltage waveforms are denoted by dashed and solid, respectively, and the simulated time-averaged applied voltage and dielectric surface potentials are shown by the dash-dotted lines. Labels A and B correspond to excitation during periods of sheath collapse and sheath expansion, respectively. Operating conditions, 100 sccm argon, plenum pressure ≈ 200 Pa (1.5 Torr), applied voltage $\phi_0 = 240$ V, fundamental frequency of $f_0 = 13.56$ MHz.

As a baseline comparison, the measured and simulated axially-integrated $\text{Ar}(2p_1)$ excitation rates and corresponding voltage waveforms for a $\phi_0 = 240$ V, 13.56 MHz discharge are shown in figures 4 (a), (d) and (g), respectively, exhibiting close agreement. For both measurement and simulation, excitation is predominately observed during phases of sheath collapse (peak A) and sheath expansion (peak B). These two excitation rate maxima arising from heating of the electron population through interactions with the radially expanding and contracting sheath (typically called α -mode heating in planar CCPs). Electron heating during the phase of sheath collapse (peak A) is particularly pronounced due to the inherent physical asymmetry within the HC geometry, necessitating an enhanced electron flux during this phase to maintain charge balance, agreeing with behaviour observed in Ref. 59. Finally, there also exists a time-averaged component to the excitation rate, arising from secondary electrons released following ion bombardment of the alumina surface, indicating a degree of γ -mode heating.

Close agreement is also observed between the measured and simulated excitation structures for the optimised $n = 5$ tailored voltage waveforms, as shown in figures 4 (b) and (c) for peak ($\theta = 90^\circ$)

waveforms and figures 4 (e) and (f), for valley ($\theta = 270^\circ$) waveforms, respectively. The excitation arising from the peak waveform in figure 4 (b), is predominately observed during the phase of sheath expansion (peak B), and to a lesser extent, the phase of sheath collapse (peak A). Notably, these excitation structures are temporally narrower and closer in phase than the single frequency case, figure 3 (a), and this arises from the reduced temporal separation between periods of significant changes in applied voltage. When comparing the measured and simulated ‘peak’ waveform excitation structures in figures 4 (b) and (e), it is apparent that sheath collapse heating (peak A) is overestimated in simulation as compared to experiment. This likely arises from an underestimation of the plasma density, leading to an exaggerated electron velocity, and hence flux, during the phase of sheath collapse as required to maintain charge continuity⁵¹.

A closer agreement is observed between the measured and simulated valley waveform excitation structures, shown in figures 4 (c) and (f), respectively. Here, electron heating via sheath collapse (peak A) and sheath expansion (peak B) are similar in both simulation and experiment. The measured and simulated voltage waveforms also exhibit a closer agreement in figure 4 (h). Of note is the significant modulation of the dc self-bias voltage between the $n = 5$ peak and valley waveforms, varying by 85% between $-213 \leq \eta_{dc} \leq -32$ V, respectively, shown in figures 4 (h) and (i). This modulation exceeds the analytically obtained 65% modulation in the voltage amplitude asymmetries, discussed with reference to figure 1 (c). The additional control arises partially from the optimization of the peak and valley waveforms shapes and partially via the plasma response to changes in the powered and grounded sheath potentials, via ϵ_s in equation 7, which varies in proportion to the ion densities adjacent to the powered and grounded electrodes. Therefore, control of the dc self-bias voltage is intrinsically linked to not only the voltage amplitude asymmetry, but also to second order effects arising from changes to the ionisation mechanisms adjacent to plasma facing surfaces.

4 Control of Ionisation Mechanisms, Sheath Dynamics and Ion Flux

Figure 5 shows the dc self-bias voltage, secondary electron ionisation rate ι_γ and radial Ar^+ ion flux Γ_{Ar^+} adjacent to the powered electrode for tailored voltage waveforms employing phase offsets in the range $0^\circ \leq \theta \leq 360^\circ$, where waveform harmonic components are computed employing equation 2. The degree to which the dc self-bias voltage is modulated for $\phi_0 = 450$ V, $n = 2$ dual-frequency and $n = 5$ tailored voltage waveforms is shown in figure 5 (a). The associated variations in the maximum secondary ionisation rate and radial Ar^+ flux, adjacent to and incident upon the alumina wall covering the powered electrode at $Z = 21$ mm, see figure 2, are shown in figures 5 (b) and (c), respectively. Phase offsets corresponding to the waveforms previously presented in figures 1 (a) and

(b) are highlighted in blue. Note that, since the peak-to-peak voltage of the waveform varies with the phase offset, the dc self-bias voltages in figure 5 (a) are normalised to the actual peak-to-peak voltage V_{pp} of each individual waveform.

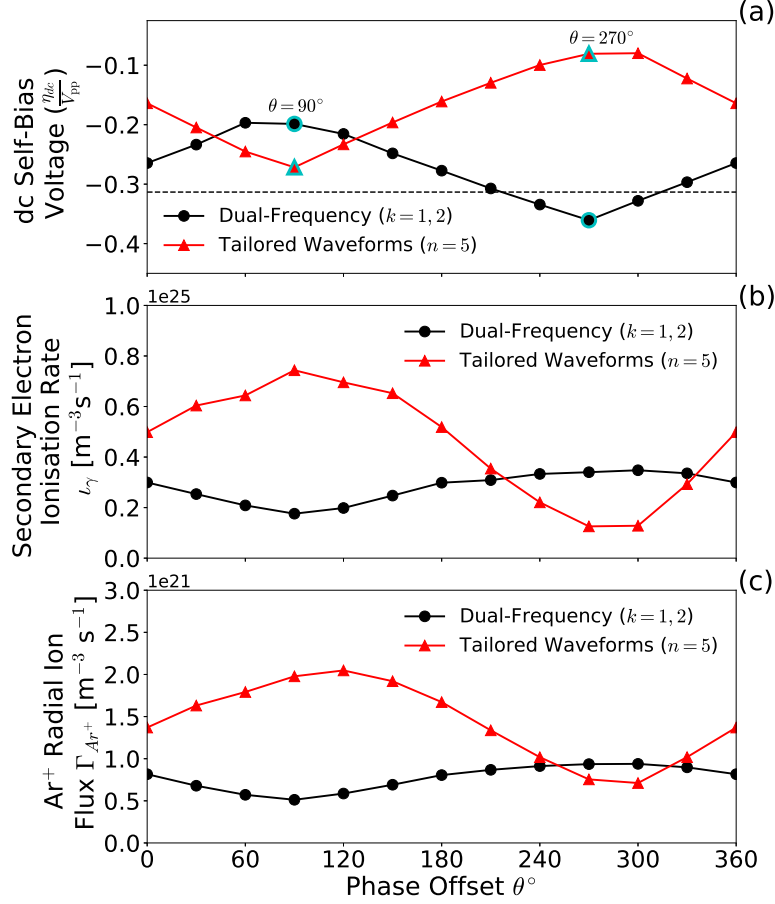


Figure 5: Phase-averaged (a) dc self-bias voltage η_{dc} , (b) secondary electron ionisation rates ν_γ and (c) radial Ar^+ fluxes Γ_{Ar^+} for unoptimised $n = 2$, $k = 1, 2$ dual-frequency and $n = 5$ tailored voltage waveforms employing phase offsets in the range $0^\circ \leq \theta \leq 360^\circ$, where waveform harmonic components are computed employing equation 2. The dc self-bias voltages in (a) are normalised to their respective peak-to-peak waveform voltage V_{pp} where $V_{pp} \leq 2\phi_0$. Phase offsets that result in the most positive and negative dc self-bias voltages are denoted by a cyan outline. Operating conditions: 100 sccm argon, plenum pressure ≈ 200 Pa (1.5 Torr), $\phi_0 = 450$ V, fundamental frequency of $f_0 = 13.56$ MHz.

Modulation of the dc self-bias voltages in 5 (a) is greatest for the $n = 5$ tailored waveforms, where $\Delta\eta_{dc} = 0.19$, as compared to $n = 2$, $k = 1, 2$ dual-frequency waveforms, where $\Delta\eta_{dc} = 0.16$, representing a 20% increase in control afforded by the $n = 5$ waveforms. While the tailored voltage waveforms exhibit the largest modulation in dc self-bias voltage, it is the dual-frequency waveforms that achieve the most negative dc self-bias voltages. Indeed, dual-frequency waveforms employing phase offsets between $240^\circ \leq \theta \leq 300^\circ$ achieve more negative dc self-bias voltages than the single frequency 13.56 MHz reference case, while the $n = 5$ tailored voltage waveforms always remain more positive than the reference discharge. At this point it should be noted that $n = 2$ and $n = 5$ multi-harmonic tailored waveforms exhibit varying degrees of destructive interference between successive

harmonics, leading to an average peak-to-peak voltage of $V_{pp} = 760$ V for the $n = 2$ voltage waveforms, a slightly lower average peak-to-peak voltage of $V_{pp} = 674$ V for the $n = 5$ voltage waveforms, while the single frequency comparison maintains a peak-to-peak voltage of $V_{pp} = 2\phi_0 = 900$ V. Despite the increased destructive interference and lower peak-to-peak voltages inherent to higher n discharges, the $n = 5$ tailored voltage waveforms still deposit the highest average power from $2.0 \leq P_{rf} \leq 7.2$ W (4.7 W average) as compared to $1.7 \leq P_{rf} \leq 4.6$ W (3.4 W average) for the $n = 2$ dual-frequency waveforms over the phase offset range $0^\circ \leq \theta \leq 360^\circ$. As a result, the $n = 5$ tailored voltage waveforms exhibited higher plasma densities adjacent to the powered electrode, between 1.5×10^{18} to 3.9×10^{18} [m⁻³] (a factor of 2.5), as compared to the dual-frequency discharges where plasma densities adjacent to the powered electrode varied between 0.8×10^{18} to 1.4×10^{18} [m⁻³] (a factor of 1.7).

The higher absolute plasma densities for the $n = 5$ discharges result in higher absolute radial Ar⁺ ion fluxes incident upon, and hence higher secondary electron ionisation rates adjacent to, the alumina surface covering the powered electrode, shown in figures 5 (b) and (c), respectively. Notably however, despite more positive dc self-bias voltages, the $n = 5$ tailored voltage waveforms still exhibit a significant modulation in these parameters, where the secondary ionisation rate and radial Ar⁺ ion flux vary by factors of 5.9 and 2.9, respectively, as compared to factors of only 1.9 and 1.8 for $n = 2$, $k = 1, 2$ dual-frequency waveforms. Typically, such modulations in the radial Ar⁺ ion flux are directly influenced by the dc self-bias voltage as required to maintain quasi-neutrality, where more negative dc self-bias voltages enforce higher positive ion fluxes³. However, the radial Ar⁺ ion flux is also indirectly influenced via the phase-resolved sheath potential (discussed with reference to figure 6 (b)) through modifying the number and energy distribution of secondary electrons that are accelerated from the alumina surface following ion bombardment¹³. For the HC discharges employed in this work, ionisations arising from secondary electron interactions typically represent between 50 – 80 % of the total ionisation rate, being greatest for phase offsets resulting in the most negative dc self-bias voltages. As a result, tailored voltage waveform shapes which increase the secondary electron ionisation adjacent to the powered electrode sheath will lead to higher ion densities and higher Ar⁺ ion fluxes, resulting in a non-linear relationship between these two parameters, as distinct from the dc self-bias voltage modulation. This non-linearity is observed for the $n = 5$ tailored voltage waveforms by the wider disparity between the modulation in secondary ionisation rate and radial flux as compared to the $n = 2$, $k = 1, 2$ dual-frequency waveforms, despite their overall more positive dc self-bias voltages. This indicates a degree of decoupling between the behavior of the ion flux incident upon the alumina wall and the dc self-bias voltage.

This behavior differs from that typically observed in tailored waveform driven, low pressure planar discharges in argon, where the ion flux typically remains relatively constant with applied upper harmonic phase offset^{15,17,43,75,79}, but is consistent with previous work in intermediate pressure non-planar geometries⁵¹, where secondary ionisation is an important ionisation mechanism. As mentioned previously with respect to equation 7, the mediator of this behavior is dictated by the degree to which the plasma response (via ϵ_s) and phase-resolved sheath dynamics adjacent to the radial wall influence the radial Ar^+ ion flux.

Figure 6 shows the phase-resolved sheath dynamics, specifically the sheath extents $S_R(\tau)$ and sheath potentials $\phi_R(\tau)$, adjacent to the powered electrode for $n = 2$, $k = 1, 2$ dual-frequency and $n = 5$ tailored voltage waveforms. Figures 6 (a) and (b) show the applied $n = 5$ peak ($\theta = 90^\circ$), valley ($\theta = 270^\circ$) and $n = 2$, $k = 1, 2$ dual-frequency voltage waveforms resulting in the most positive and negative dc self-bias voltages as previously shown in figure 5 (a). The associated phase-resolved radial sheath extents and sheath potentials are presented for the peak and valley waveforms in figures 6 (c), and (e), and for the dual-frequency waveforms in figures 6 (d), and (f), respectively. All waveforms in figure 6 employ harmonic components as computed employing equation 2. The sheath extents in figures (c) and (d) were obtained via the Brinkmann criterion⁶² and smoothed employing a Savitzky-Golay filter. The horizontal dashed lines in figures (c-f) denote the phase-averaged values of their respective parameters for clarity.

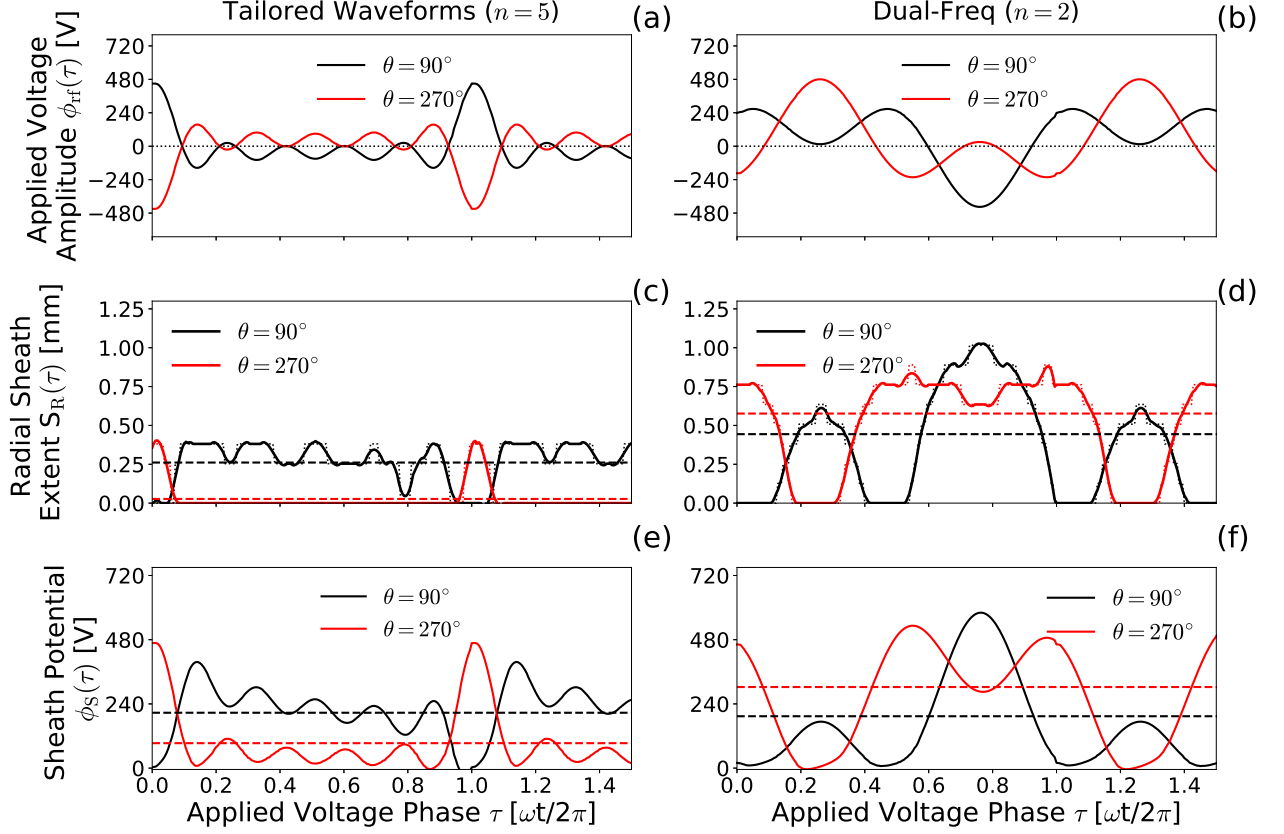


Figure 6: Phase-resolved (a),(b) electrode voltage waveforms ϕ_{rf} , (c),(d), radial sheath extents $S_R(\tau)$ and (e),(f) sheath potentials $\phi_s(\tau)$ for unoptimised $n = 2$, dual-frequency and $n = 5$ tailored voltage waveforms, respectively, where waveform harmonic components are computed employing equation 2. Waveforms employing phase offsets of $\theta = 90^\circ$ and $\theta = 270^\circ$ represent the extrema in dc self-bias voltages as previously shown in figure 5 (a). Sheath extents and potentials presented in panels (c),(d), and (e),(f) are obtained adjacent to the radial wall at the axial mid-point of the powered electrode at $Z = 21$ mm. Waveforms are presented between rf phases $0.0 \leq \tau \leq 1.5$ for clarity. Operating conditions: 100 sccm argon, plenum pressure ≈ 200 Pa (1.5 Torr), $\phi_0 = 450$ V, fundamental frequency of $f_0 = 13.56$ MHz.

The powered electrode voltage waveforms in figures 6 (a) and (b) are as previously presented in figures 1 (a) and (b), shown between rf phases $0.0 \leq \tau \leq 1.5$ for clarity, and represent the discharges achieving the most negative ($\theta = 90^\circ$) and positive ($\theta = 270^\circ$) dc self-bias voltages, respectively. Both the $n = 5$ peak and valley voltage waveforms exhibit a relatively low amplitude for the majority of the rf phase cycle, exhibiting a single positive or negative voltage spike between $0.9 \leq \tau \leq 1.1$. In comparison, the dual-frequency voltage waveforms possess a smoothly varying voltage throughout the rf cycle, exhibiting a single relatively-wide change in amplitude at either $\tau = 0.75$ or $\tau = 1.25$, for phase offsets of $\theta = 90^\circ$ or $\theta = 270^\circ$, respectively.

The radial sheath extents in figures 6 (c) and (d) exhibit a significant variation for operation employing $n = 5$ tailored voltage waveforms, being modulated by a factor of 8.66, from 0.03 mm to 0.29 mm, for valley ($\theta = 270^\circ$) and peak ($\theta = 90^\circ$) waveforms, respectively. By comparison, $n = 2$ dual-frequency waveforms achieve sheath extent modulations by a factor of only 1.56, from 0.44 mm

to 0.58 mm, for $\theta = 90^\circ$ and $\theta = 270^\circ$, respectively. This disparity arises due to the varying amplitude asymmetry of the applied voltage waveforms, specifically the temporal extent of the maximum and minimum voltage amplitudes within each waveform. Higher harmonic $n = 5$ tailored waveforms exhibit significantly temporally narrower extrema in voltage amplitude, see figure 6 (a), enabling operation in regimes where the powered electrode sheath is either expanded or collapsed for $\approx 90\%$ of the rf phase cycle. In addition, the higher Ar^+ ion densities afforded via the enhanced secondary electron ionisation rate leads to generally reduced sheath extents for the $n = 5$ tailored voltage waveforms. Such enhanced control of the sheath extent is of particular interest in intermediate and high pressure plasmas, where ion-ion and ion-neutral collisions in the sheath represent a significant ion energy loss mechanism.

In addition to enhanced control of the phase-averaged sheath extent, $n = 5$ tailored voltage waveforms also exhibit a significant modulation of the sheath potential, shown in figure 6 (e), where the average sheath potential ϕ_S varies by a factor of 2.3 between 93 V to 207 V from $\theta = 270^\circ$ to $\theta = 90^\circ$. This level of control is not matched by the dual-frequency voltage waveforms where the sheath potential varies more smoothly in figure 6 (f), resulting in a reduced modulation fraction of 1.6, between 194 V to 303 V over the same phase offset range. The sheath potentials for $n = 5$ tailored waveforms being lower on average than the $n = 2$, $k = 1, 2$ dual-frequency waveforms due to the generally more positive dc self-bias voltages, shown previously in figure 5 (a). Notably, in both cases the variation in sheath potential is significantly larger than the variation in the plasma potential ϕ_p , with $n = 5$ tailored waveforms varying ϕ_p by only 20 % between 42 V to 51 V and $n = 2$ dual-frequency waveforms varying ϕ_p by 14 % from 50 V to 58 V. The plasma potential is maintained relatively constant due primarily to the inverse relationship between the dc self-bias voltage and the on-axis plasma density. Phase offsets resulting in the most negative dc self-bias voltages, which would typically reduce the plasma potential, also result in the highest plasma densities, increasing the plasma potential, resulting in a stabilising effect⁴¹. The opposite is true of phase offsets which result in positive dc self-bias voltages. This indicates that both types of waveforms primarily influence the sheath potential through modifying the dielectric surface voltage (dc self-bias voltage), which itself varies in proportion to the applied voltage $\phi_{rf}(t)$ and hence inherits the voltage amplitude asymmetry of the supplied rf voltage waveform, shown previously in figure 1 (c). Therefore, any variation in the phase-averaged sheath potential is primarily influenced by the maximum voltage drop across sheath each via equation 5, and the voltage waveform amplitude asymmetry via equation 7.

5 Control of Ion Energy Distribution Functions

Figures 7 (a) and (b) show the Ar^+ IEDFs incident on the radial wall adjacent to the powered electrode ($R, Z = 2.1, 21$ mm) for $n = 2, k = 1, 2$ dual-frequency and $n = 5$ tailored voltage waveforms, respectively, employing phase offsets in the range $0^\circ \leq \theta \leq 360^\circ$ on the vertical-axis, where waveform harmonic components are computed employing equation 2. IEDFs are integrated for angles of incidence up to 45° symmetrically about the normal, and are normalised such that the integral over all energies ϵ is equal to unity. The mean $\bar{\epsilon}$ and modal $\bar{\epsilon}$ Ar^+ ion energies for each phase offset are denoted by the dashed black and white lines, respectively, and phase offsets corresponding to the most positive and negative dc self-bias voltages are denoted by the horizontal red and blue dashed lines, respectively.

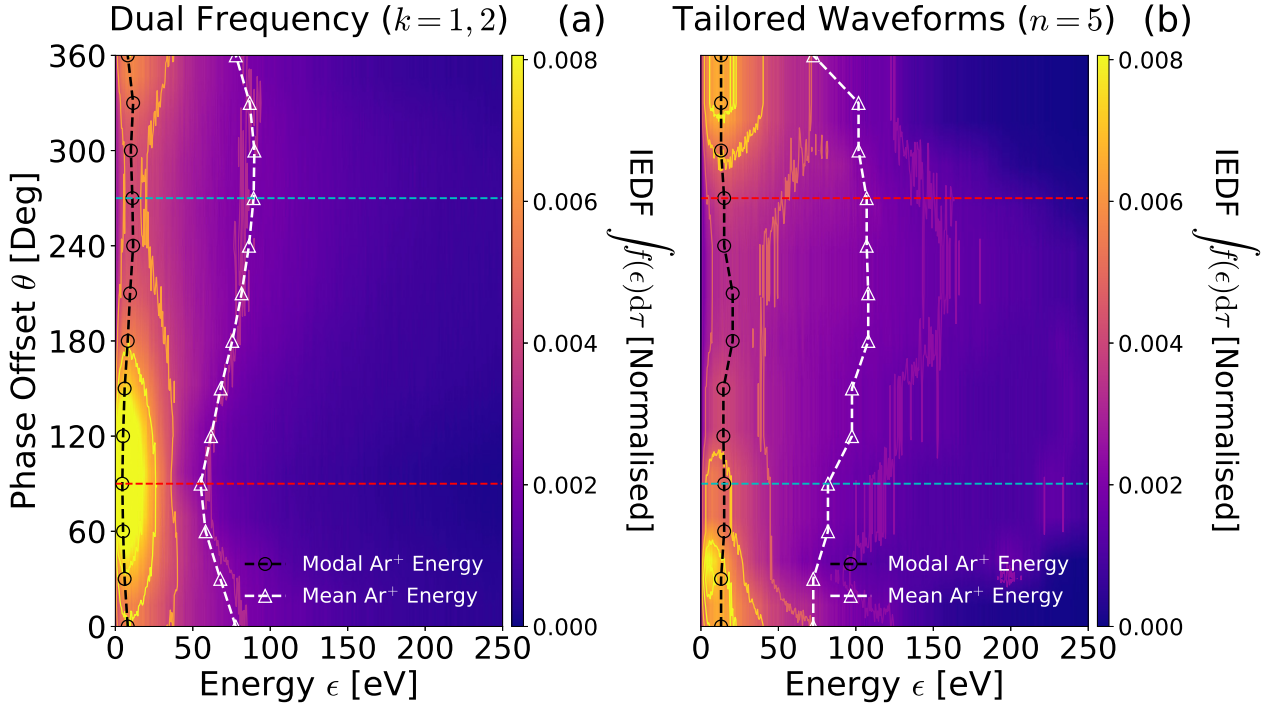


Figure 7: IEDF at the radial wall adjacent to the powered electrode ($R, Z = 2.1$ mm, 21 mm) for (a) unoptimised $n = 2, k = 1, 2$ dual-frequency and (b) $n = 5$ tailored voltage waveforms employing phase offsets in the range $0^\circ \leq \theta \leq 360^\circ$, where waveform harmonic components are computed employing equation 2. The mean $\bar{\epsilon}_{\text{Ar}^+}$ and modal $\bar{\epsilon}_{\text{Ar}^+}$ Ar^+ ion energies for each phase offset are denoted by the black circles and white triangles, respectively, where connecting lines are added to guide the eye. Phase offsets that correspond to the most positive and negative dc self-bias voltages are denoted by dashed red and blue lines, respectively. Operating conditions: 100 sccm argon, plenum pressure ≈ 200 Pa (1.5 Torr), $\phi_0 = 450$ V, fundamental frequency of $f_0 = 13.56$ MHz.

Variation in the IEDF incident upon the alumina surface is observed for operation employing both $n = 2, k = 1, 2$ dual-frequency and $n = 5$ tailored voltage waveforms, shown in figures 7 (a) and (b). All dual-frequency IEDFs exhibit shapes consistent with a collisionally dominated sheath ($\lambda_{\text{mfp}} \leq S_R$) as would be expected given the relatively wide phase averaged sheath extents, shown previously in figure 6 (d). An elongated tail of fast ions (up to 500 eV) were observed for all $n = 2$ discharges,

arising during the phases of most negative applied voltage, where the sheath potential can exceed 500 V, see figure 6 (f). Dual-frequency voltage waveforms exhibit a moderate degree of control over the shape of the IEDF, modulating the mean ion energy by 35 eV between $55.0 \leq \hat{\epsilon}_{Ar+} \leq 90.0$ eV and the modal ion energy by 7 eV between $4.5 \leq \bar{\epsilon}_{Ar+} \leq 11.5$ eV. Maximum mean and modal ion energies are observed for $\theta = 270^\circ$, corresponding to the most negative dc self-bias in figure 5 (a), as would be expected from equation 8. It is also useful to note here that the neutral gas temperature, and hence neutral gas density and ion mean-free-path, vary with respect to applied phase offset. This has the added effect of slightly reducing collisional losses (and hence increasing mean ion energies) for phase offsets which result in the highest neutral gas heating, i.e. those with the most negative dc self-biases, corresponding to the blue dashed lines.

In comparison, IEDFs resulting from discharges employing $n = 5$ tailored voltage waveforms, while still predominately collisional in nature, exhibit more notable populations of high energy ($\geq \hat{\epsilon}$) ions. These super-thermal ions are most prominent for waveforms employing phase offsets in the range $90^\circ \leq \theta \leq 270^\circ$, resulting in an enhanced separation between the mean and modal ion energies. These super-thermal ion populations arise as the phase-averaged sheath widths, observed previously in figure 6 (c), fall below the ion mean-free-path, leading to collisionless acceleration through the sheath¹³. Despite achieving higher average ion energies, the $n = 5$ tailored voltage waveforms exhibit a similar degree of control over the IEDF, modulating the mean ion energy by 35.5 eV between $72.5 \leq \hat{\epsilon}_{Ar+} \leq 108.0$ eV and the modal ion energy by 7.5 eV between $13.0 \leq \bar{\epsilon}_{Ar+} \leq 20.5$ eV. Notably however, phase offsets resulting in the extrema in mean and modal ion energy for $n = 5$ tailored waveforms in 7 (b) do not align with phase offsets resulting in the extrema in dc self-bias voltage and sheath potential, shown previously in figures 5 (a) and 6 (e). Instead the maximum ion energies are observed for phase offsets centred around $\theta = 180^\circ$ and minimum ion energies are observed for phase offsets centred around $\theta = 0^\circ$, approximately 90° degrees out of phase from what would be expected given the trends in dc self-bias voltage and sheath potential. This offset is not observed for operation employing $n = 2$ dual-frequency voltage waveforms.

The offset between the extrema in dc self-bias voltage and extrema in ion energy for $n = 5$ tailored voltage waveforms is explained through recalling that the radial sheath extent varies in proportion to the sheath potential, shown previously in figures figure 6 (c) and (e) for $n = 5$ tailored waveforms and figure 6 (d) and (f) for $n = 2$ dual-frequency waveforms. This implies that waveforms employing phase offsets for which ions are accelerated through the largest potential are also waveforms for which ions experience the greatest collisional energy loss through the sheath. Conversely, ions accelerated through a narrow sheath are subject to fewer collisions but are accelerated through significantly reduced sheath

potential, reducing their maximum attainable energy. Therefore, the optimal conditions are found between these two extremes, agreeing with the $\approx 90^\circ$ offset observed in figure 7 (b). This behaviour is only expected for intermediate-to-high pressure plasmas ($\gtrsim 133$ Pa, 1.0 Torr), where collisional ion energy loss within the sheath is a significant factor. This effect is not observed for dual-frequency voltage waveforms due to their wider and less variable phase averaged sheath extents, observed previously in figure 6 (d). Dual-frequency waveforms therefore maintain a correlation between the extrema in dc self-bias voltage and mean ion energy for collisional sheath conditions.

5.1 Decoupling Ion Flux and Ion Energy at Intermediate Pressures

Before addressing the extent to which the ion flux and ion energy can be de-coupled in intermediate pressure, non-planar plasmas, it is useful to first identify why these parameters are coupled in single frequency discharges. Consider the energy gained by a positive ion, initially at rest, falling from a radius r through a phase-averaged sheath potential of ϕ_S . For collisional plasmas where $\lambda_{\text{mfp}} \leq S_R$, the average distance over which an ion can be continuously accelerated is equal to the mean-free-path. Therefore, for maximum energy gain, an ion would start at a radius from the alumina wall $r = \lambda_{\text{mfp}}$, resulting in an energy gain as described by equation 8.

$$\epsilon_{\text{max}} = Ze\phi_S(r) \quad (8)$$

Here, ϵ_{max} is the maximum achievable ion energy before a scattering event, Z is the ionisation level of the accelerated ion, and e is the elementary charge; where both Z and e are constant. For the case where the sheath potential varies primarily in proportion to the plasma potential, i.e. where the dc self-bias voltage is zero or constant, any variation in the maximum ion energy must arise from a change to either its mean-free-path or to the sheath width, and hence potential gradient. To a first order approximation, these parameters vary in inverse proportion to the local neutral and ion densities, respectively³. For cases where the change in neutral argon density is negligible, the expected maximum ion energy can be mainly defined by the ion density, and hence is proportional to the ion flux.

The introduction of a variable dc self-bias voltage, such as provided by multi-harmonic voltage waveforms, breaks this co-dependency between the ion density and ion energy through enabling modulation of the sheath potential independent of the ion density. Independent control of ion energy and ion flux is then possible so long as the ion flux does not respond significantly to changes in the dc self-bias voltage, as is typically the case for low pressure, planar discharges^{43,75,79}. However, in general this cannot be assumed for intermediate pressure or non-planar plasma sources, as demonstrated in

figure 5 (b) and (c), due to changes in the ion flux arising from secondary ionisation mechanisms, or through pre-existing physical asymmetries, which enforce significant variations in the ion fluxes required for quasi-neutrality¹⁹. Independent control of the ion energy and flux in collisional or intrinsically asymmetric discharges therefore arises from the offset between the extrema in ion energy as compared to the extrema in ion flux in response to changes to the dc self-bias voltage. The degree to which these two parameters are offset in response to the dc self-bias voltage is mediated by the behaviour of the sheath extent and sheath potential, discussed previously with reference to figures 6 (c) and (e).

The degree of independent control over the mean Ar^+ ion energy and flux afforded by $n = 2$, $k = 1, 2$ dual-frequency and $n = 5$ tailored voltage waveforms is presented in figure 8, for phase offsets between $0^\circ \leq \theta \leq 360^\circ$, where waveform harmonic components are computed employing equation 2. Single frequency discharges employing driving frequencies of 13.56 MHz, 54.24 MHz and 108.36 MHz with applied voltages in the range $150 \leq \phi_0 \leq 450$ V are included for comparison, where the data underpinning the single frequency trends is reproduced from Ref. 13.

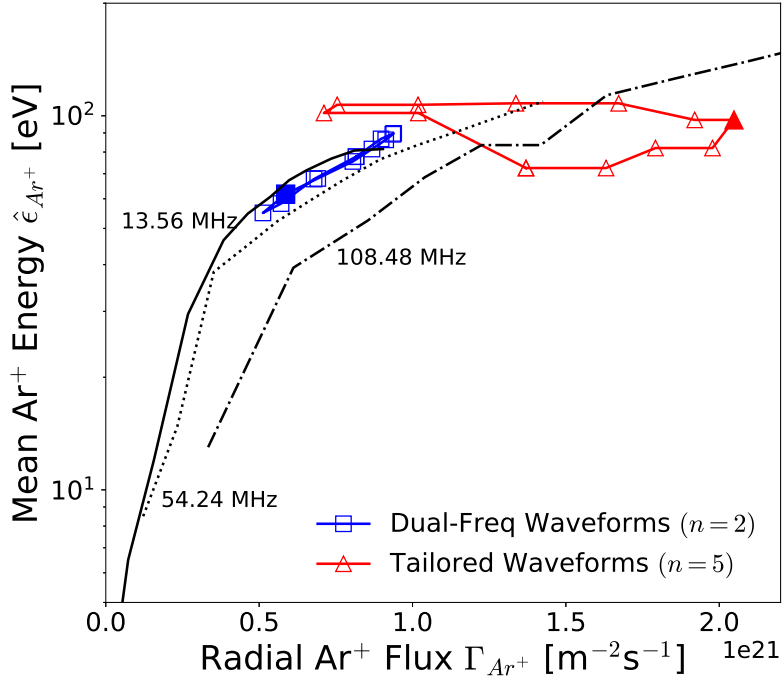


Figure 8: Mean Ar^+ ion energies $\hat{\epsilon}_{\text{Ar}^+}$ incident upon the radial wall adjacent to the powered electrode ($R, Z = 2.1, 21$ mm) with respect to the Ar^+ ion flux Γ_{Ar^+} at the same location employing unoptimised $n = 2, k = 1, 2$ dual-frequency and $n = 5$ tailored voltage waveforms with phase offsets $0^\circ \leq \theta \leq 360^\circ$, where waveform harmonic components are computed employing equation 2. Single frequency discharges are included for comparison employing driving frequencies of 13.56 MHz, 54.24 MHz and 108.36 MHz with applied voltages $150 \leq \phi_0 \leq 450$ V, where data is reproduced from Ref. 13. Increasing phase offset proceeds clockwise, with waveforms employing a phase offset of 90° denoted by the filled shapes as a reference. Operating conditions: 100 sccm argon, plenum pressure ≈ 200 Pa (1.5 Torr), multi-harmonic waveforms $\phi_0 = 450$ V, single frequency waveforms $150 \leq \phi_0 \leq 450$ V in steps of 30 V, fundamental frequency of $f_0 = 13.56$ MHz.

For single frequency operation, denoted by the black solid, dashed and dotted lines in figure 8, the ion flux Γ_{Ar+} and mean ion energy $\hat{\epsilon}_{Ar+}$ both vary in proportion with the ion density, as described previously with reference to equation 8. This results in a uniquely defined locus of possible ion flux, mean ion energy combinations for any given single frequency discharge, assuming a fixed voltage amplitude and background pressure¹². The application of additional frequencies provides a degree of mobility in flux-energy space, i.e. enabling multiple ion flux, mean ion energy combinations, achieved by modulating the dc self-bias via varying harmonic phase offsets. This is demonstrated in figure 8, where both dual-frequency and $n = 5$ tailored waveforms exhibit modulations in flux-energy space.

Dual-frequency voltage waveform driven discharges in figure 8 exhibit an approximately linear modulation in flux-energy space, cycling clockwise around a point in-between the 13.56 MHz and 54.24 MHz trend lines with increasing phase offset. This modulation is narrower in energy than flux, where the radial ion flux is modulated by a factor of 1.8, as compared to a factor of 1.6 for the mean ion energy. As the modulation in ion energy and flux both vary in proportion to the magnitude of the dc self bias voltage, noted previously in figures 5 (c) and 7 (b), the achieved mobility in flux-energy space is very low. This behaviour differs from previous work performed in low pressure ($\lesssim 67$ Pa, 0.5 Torr), planar rf-CCPs operating in Ar, where typically the ion flux remains near-constant and the ion energy is independently variable^{15,17,43,75,79}.

In comparison, tailored voltage waveforms achieve modulations in Ar^+ ion flux Γ_{Ar+} and mean ion energy $\hat{\epsilon}_{Ar+}$ by factors of 2.9 and 1.5, respectively. Further, as the ion energy is not modulated in direct proportion to the dc self-bias voltage, shown previously in figure 7 (b), the achieved mobility in flux-energy space is significantly increased. This enables multiple distinct ion energy and ion flux combinations e.g. a high flux, mid energy configuration ($\theta = 90^\circ$) and a low flux, mid energy configuration ($\theta = 270^\circ$). Higher harmonic tailored voltage waveforms therefore re-enable variation of the ion energy, while maintaining a near constant ion flux in non-planar, intermediate pressure rf-CCP sources. Finally, it is worth noting that the degree of control achieved in figure 8 may be further optimised through the application of waveforms employing optimised harmonic amplitudes of the form described by equation 3.

The extent to which ion energy and flux may be varied independently can be quantitatively described by the Pearson correlation coefficient^{80,81} $\rho(\epsilon, \Gamma)$, with respect to the applied phase offset, and is computed as shown in equation 9:

$$\rho(\epsilon, \Gamma) = \frac{\text{Cov}(\hat{\epsilon}_{Ar+}, \Gamma_{Ar+})}{\sigma(\hat{\epsilon}_{Ar+})\sigma(\Gamma_{Ar+})} \quad (9)$$

Where $\text{Cov}(\hat{\epsilon}_{Ar+}, \Gamma_{Ar+})$ is the covariance between mean ion energy and radial ion flux⁸⁰:

$$\text{Cov}(\hat{\epsilon}_{Ar+}, \Gamma_{Ar+}) = \text{Mean}\{(\hat{\epsilon}_{Ar+}(\theta) - \langle \hat{\epsilon} \rangle_{Ar+}) \times (\langle \Gamma \rangle_{Ar+} - \Gamma_{Ar+}(\theta))\} \quad (10)$$

Here, $\langle \hat{\epsilon} \rangle_{Ar+}$ and $\langle \Gamma \rangle_{Ar+}$ represent the ensemble average values of mean ion energy and ion flux averaged over all phase offsets in the range $0^\circ \leq \theta \leq 360^\circ$, and $\sigma(\hat{\epsilon}_{Ar+})$ and $\sigma(\Gamma_{Ar+})$ are the standard deviations over the same phase offset range. While $\hat{\epsilon}_{Ar+}(\theta)$ and $\Gamma_{Ar+}(\theta)$, represent the mean ion energy and ion flux for a specific value of θ , and are otherwise functionally equivalent to the symbols $\hat{\epsilon}_{Ar+}$ and Γ_{Ar+} . The correlation coefficient is a normalised parameter, such that $-1 \leq \rho(\epsilon, \Gamma) \leq 1$, where the magnitude denotes the degree of linear correlation, with either a direct or indirect proportionality for positive and negative values, respectively. Note that a correlation coefficient of zero denotes no correlation, i.e. independent behavior, between the two parameters.

Computing correlation coefficients for the single frequency trends shown in figure 8, it can be shown that $+0.997 \geq \rho(\epsilon, \Gamma) \geq +0.989$ for single frequency operation in the range 108.68 MHz to 13.56 MHz, respectively. Note the directly proportional relationship between ion flux and mean ion energy, as would be expected from equation 8. Note also that higher driving frequencies lead to increasingly linear correlations, which is likely a result of increased gas heating and reduced collisionality within the powered electrode sheath⁵¹.

The application of $n = 2, k = 1, 2$ dual-frequency waveforms produces a negligible change in correlation coefficient as compared to the 13.56 MHz case, varying from $\rho(\epsilon, \Gamma) = +0.989$ to $\rho(\epsilon, \Gamma) = +0.995$. This indicates that, while dual-frequency operation does provide control over the ion flux and ion energy, demonstrated in figures 5 (c) and 7 (a), this control does not lead to any significant decoupling of these two parameters under the intermediate pressure conditions studied here. In contrast, the application of $n = 5$ tailored voltage waveforms reduces the correlation coefficient by a factor of ≈ 3 to $\rho(\epsilon, \Gamma) = +0.373$, demonstrating a significant increase in the independent variability of the mean ion energy and ion flux. This agrees with the observed elliptical modulation in flux-energy space achieved via $n = 5$ tailored voltage waveforms in figure 8, as compared to linear modulations both single-frequency and dual-frequency voltage waveforms. These findings suggest that the application of the EAE via tailored voltage waveforms to intermediate-to-high pressure, non-planar discharge configurations is not identical to that in the planar geometry. In particular, achieving specific plasma parameters (e.g. a high flux, low energy configuration) is not possible through maximizing the potential drop through a single sheath via application of dual-frequency voltage waveforms, as in planar dis-

charges. Instead, the sheath dynamics, sheath voltage and spatio-temporal electron heating dynamics are simultaneously modulated by the applied tailored voltage waveform, necessitating a consideration of the plasma response to the applied waveform within the numerical approach. Such considerations are essential to future works employing the EAE via tailored voltage waveforms in asymmetric, non-planar discharges.

6 Conclusions

To conclude, quasi-independent control of the radial Ar^+ flux and mean Ar^+ ion energy has been demonstrated via 2D fluid/Monte-Carlo simulations of a $\phi_0 = 450$ V, $n = 5$ tailored voltage waveform driven hollow cathode micro-discharge operating in argon at ≈ 200 Pa, 1.5 Torr plenum pressure. Close agreement between simulated and measured $\text{Ar}(2p_1)$ excitation rates was observed for $\phi_{rf} = 240$ V $n = 5$ tailored voltage waveforms employing phase-offsets of $\theta = 90^\circ$ and $\theta = 270^\circ$ and further simulations are used to investigate trends over the range $0^\circ \leq \theta \leq 360^\circ$. By virtue of more finely grained temporal features, $n = 5$ tailored voltage waveforms achieved modulations in the phase-averaged powered electrode sheath extent and potential by factors of 8.66 and 2.23, respectively, as compared to only 1.56 and 1.32 for $n = 2$ dual-frequency voltage waveforms. This led to a significantly increased degree of independent control over the ion flux Γ_{Ar^+} and mean ion energy $\bar{\epsilon}_{\text{Ar}^+}$, modulating each by factors of 2.9 and 1.6, respectively, as compared to 1.8 and 1.6 for $n = 2$ dual-frequency waveforms. Notably, these trends demonstrated a reducing correlation between the ion flux and mean ion energy with increasing tailored waveform harmonic, from $\rho(\epsilon, \Gamma) = +0.989$ for 13.56 MHz single frequency operation to $\rho(\epsilon, \Gamma) = +0.373$ for operation employing $n = 5$ tailored voltage waveforms. Multi-harmonic $n \geq 2$ tailored voltage waveforms therefore represent an effective technique for the control of ion dynamics in intermediate pressure ($\gtrsim 133$ Pa 1 Torr), physically asymmetric radio-frequency capacitively coupled plasma sources, finding application in aerospace and semiconductor industries.

7 Acknowledgements

The authors wish to thank M. J. Kushner for provision of the HPEM code and ongoing support, P. Hill, R. Armitage and K. Niemi for technical support, T. Gans and D. O'Connell for fruitful discussions and S. Dine for technical support relating to the Solayl sensor. The work presented herein was partially funded by the Engineering and Physical Sciences Research Council (EPSRC), grant reference number: EP/m508196/1.

8 References

- [1] I Adamovich, S D Baalrud, A Bogaerts, P J Bruggeman, M Cappelli, V Colombo, U Czarnetzki, U Ebert, J G Eden, P Favia, D B Graves, S Hamaguchi, G Hieftje, M Hori, I D Kaganovich, U Kortshagen, M J Kushner, N J Mason, S Mazouffre, S Mededovic Thagard, H R Metelmann, A Mizuno, E Moreau, A B Murphy, B A Niemira, G S Oehrlein, Z Lj Petrovic, L C Pitchford, Y K Pu, S Rauf, O Sakai, S Samukawa, S Starikovskaia, J Tennyson, K Terashima, M M Turner, M C M Van De Sanden, and A Vardelle. The 2017 Plasma Roadmap: Low temperature plasma science and technology. *Journal of Physics D: Applied Physics*, 50(32):323001, 2017. ISSN 13616463. doi:[10.1088/1361-6463/aa76f5](https://doi.org/10.1088/1361-6463/aa76f5).
- [2] S Samukawa, M Hori, S Rauf, K Tachibana, P Bruggeman, G Kroesen, J C Whitehead, A B Murphy, A F Gutsol, S Starikovskaia, U Kortshagen, J.-P. Boeuf, T J Sommerer, M J Kushner, U Czarnetzki, and N Mason. The 2012 Plasma Roadmap. *Journal of Physics D: Applied Physics*, 45(25):253001, 2012. ISSN 0022-3727. doi:[10.1088/0022-3727/45/25/253001](https://doi.org/10.1088/0022-3727/45/25/253001).
- [3] M A Lieberman and A J Lichtenberg. *Principles of Plasma Discharges and Materials Processing*. John Wiley & Sons, New Jersey, 2nd edition, 2005. ISBN 0-471-72001-1. doi:[10.1017/CBO9781107415324.004](https://doi.org/10.1017/CBO9781107415324.004).
- [4] L Bárdoš. Radio frequency hollow cathodes for the plasma processing technology. *Surface and Coatings Technology*, 86-87(PART 2):648–656, 1996. ISSN 02578972. doi:[10.1016/S0257-8972\(96\)03056-3](https://doi.org/10.1016/S0257-8972(96)03056-3).
- [5] K J Kanarik, T Lill, E A Hudson, S Sriraman, S Tan, J Marks, V Vahedi, and R A Gottscho. Overview of atomic layer etching in the semiconductor industry. *Journal of Vacuum Science & Technology A: Vacuum, Surfaces, and Films*, 33(2):20802, 2015. ISSN 0734-2101. doi:[10.1116/1.4913379](https://doi.org/10.1116/1.4913379).
- [6] G. Cunge, M. Kogelschatz, O. Joubert, and N. Sadeghi. Plasma-wall interactions during silicon etching processes in high-density HBr/Cl₂/O₂ plasmas. *Plasma Sources Science and Technology*, 14(2):S42, 2005. ISSN 09630252. doi:[10.1088/0963-0252/14/2/S06](https://doi.org/10.1088/0963-0252/14/2/S06).
- [7] K R Williams, K Gupta, and M Wasilik. Etch Rates for Micromachining Processing II. *Journal of Microelectromechanical systems*, 12(6):761–777, 2003. ISSN 1098-6596. doi:[10.1017/CBO9781107415324.004](https://doi.org/10.1017/CBO9781107415324.004).
- [8] D. J. Economou. Pulsed plasma etching for semiconductor manufacturing. *Journal of Physics D: Applied Physics*, 47(30):303001, 2014. ISSN 13616463. doi:[10.1088/0022-3727/47/30/303001](https://doi.org/10.1088/0022-3727/47/30/303001).
- [9] M E Day, M Delfino, and S Salimian. Low energy ion etching of aluminum oxide films and native aluminum oxide. *Journal of Applied Physics*, 72(11):5467–5470, 1992. ISSN 00218979. doi:[10.1063/1.351990](https://doi.org/10.1063/1.351990).
- [10] S B Wang and A E Wendt. Control of ion energy distribution at substrates during plasma processing. *Journal of Applied Physics*, 88(2):643–646, 2000. ISSN 00218979. doi:[10.1063/1.373715](https://doi.org/10.1063/1.373715).
- [11] Noah Hershkowitz and Robert A. Breun. Diagnostics for plasma processing (etching plasmas). *Review of Scientific Instruments*, 68(1):880–885, 1997. ISSN 00346748. doi:[10.1063/1.1147752](https://doi.org/10.1063/1.1147752).
- [12] A Perret, P Chabert, J Jolly, and J P Booth. Ion energy uniformity in high-frequency capacitive discharges. *Applied Physics Letters*, 86(2):10–13, 2005. ISSN 00036951. doi:[10.1063/1.1848183](https://doi.org/10.1063/1.1848183).

- [13] S J Doyle, A R Gibson, R W Boswell, C Charles, and J P Dedrick. Inducing locally structured ion energy distributions in intermediate-pressure plasmas Inducing locally structured ion energy distributions in intermediate-pressure plasmas. *Physics of Plasmas*, 7(July):73519, 2019. doi:[10.1063/1.5111401](https://doi.org/10.1063/1.5111401).
- [14] B G Heil, U Czarnetzki, R P Brinkmann, and T Mussenbrock. On the possibility of making a geometrically symmetric RF-CCP discharge electrically asymmetric. *Journal of Physics D: Applied Physics*, 41(16):165202, 2008. ISSN 0022-3727. doi:[10.1088/0022-3727/41/16/165202](https://doi.org/10.1088/0022-3727/41/16/165202).
- [15] J Schulze, E Schüngel, Z Donkó, and U Czarnetzki. The electrical asymmetry effect in multi-frequency capacitively coupled radio frequency discharges. *Plasma Sources Science and Technology*, 20(1):15017, 2011. ISSN 09630252. doi:[10.1088/0963-0252/20/1/015017](https://doi.org/10.1088/0963-0252/20/1/015017).
- [16] T Lafleur and J.-P. Booth. Control of the ion flux and ion energy in CCP discharges using non-sinusoidal voltage waveforms. *Journal of Physics D: Applied Physics*, 45(39):395203, 2012. ISSN 0022-3727. doi:[10.1088/0022-3727/45/39/395203](https://doi.org/10.1088/0022-3727/45/39/395203).
- [17] T Lafleur, R W Boswell, and J.-P. Booth. Enhanced sheath heating in capacitively coupled discharges due to non-sinusoidal voltage waveforms. *Applied Physics Letters*, 100(19):194101, 2012. ISSN 00036951. doi:[10.1063/1.4712128](https://doi.org/10.1063/1.4712128).
- [18] B Bruneau, T Novikova, T Lafleur, J.-P. Booth, and E V Johnson. Control and optimization of the slope asymmetry effect in tailored voltage waveforms for capacitively coupled plasmas. *Plasma Sources Science and Technology*, 24:15021, 2015. ISSN 0963-0252. doi:[10.1088/0963-0252/24/1/015021](https://doi.org/10.1088/0963-0252/24/1/015021).
- [19] T Lafleur. Tailored-waveform excitation of capacitively coupled plasmas and the electrical asymmetry effect. *Plasma Sources Science and Technology*, 25(1):13001, 2016. ISSN 0963-0252. doi:[10.1088/0963-0252/25/1/013001](https://doi.org/10.1088/0963-0252/25/1/013001).
- [20] A R Gibson and T Gans. Controlling plasma properties under differing degrees of electronegativity using odd harmonic dual frequency excitation. *Plasma Sources Science and Technology*, 26(11):115007, 2017. ISSN 13616595. doi:[10.1088/1361-6595/aa8dcd](https://doi.org/10.1088/1361-6595/aa8dcd).
- [21] J Schulze, E Schüngel, U Czarnetzki, and Z Donko. Optimization of the electrical asymmetry effect in dual-frequency capacitively coupled radio frequency discharges: Experiment, simulation, and model. *Journal of Applied Physics*, 106(6):92005, 2009. ISSN 00218979. doi:[10.1063/1.3223310](https://doi.org/10.1063/1.3223310).
- [22] T Lafleur, P Chabert, M M Turner, and J P Booth. Theory for the self-bias formation in capacitively coupled plasmas excited by arbitrary waveforms. *Plasma Sources Science and Technology*, 22(6):65013, 2013. ISSN 0963-0252. doi:[10.1088/0963-0252/22/6/065013](https://doi.org/10.1088/0963-0252/22/6/065013).
- [23] P. Chabert and N. Braithwaite. *Physics of Radio-Frequency Plasmas*. Cambridge University Press, Cambridge, 3rd edition, 2014.
- [24] A R Gibson, A Greb, W G Graham, and T Gans. Tailoring the nonlinear frequency coupling between odd harmonics for the optimisation of charged particle dynamics in capacitively coupled oxygen plasmas. *Applied Physics Letters*, 106(5):54102, 2015. ISSN 00036951. doi:[10.1063/1.4907567](https://doi.org/10.1063/1.4907567).
- [25] B Bruneau, T Gans, D O'Connell, A Greb, E V Johnson, and J.-P. Booth. Strong Ionization Asymmetry in a Geometrically Symmetric Radio Frequency Capacitively Coupled Plasma Induced by Sawtooth Voltage Waveforms. *Physical Review Letters*, 114(12):125002, 2015. ISSN 0031-9007. doi:[10.1103/PhysRevLett.114.125002](https://doi.org/10.1103/PhysRevLett.114.125002).

- [26] A R Gibson, Z Donkó, L Alelyani, L Bischoff, G Hübner, J Bredin, S J Doyle, I Korolov, K Niemi, T Mussenbrock, P Hartmann, J P Dedrick, J Schulze, T Gans, and D O Connell. Disrupting the spatio-temporal symmetry of the electron dynamics in atmospheric pressure plasmas by voltage waveform tailoring. 28:01LT01, 2019. doi:[10.1088/1361-6595/aaf535](https://doi.org/10.1088/1361-6595/aaf535).
- [27] Z. Donkó, A. Derzsi, M. Vass, J. Schulze, E. Schuengel, and S. Hamaguchi. Ion energy and angular distributions in low-pressure capacitive oxygen RF discharges driven by tailored voltage waveforms. *Plasma Sources Science and Technology*, 27(10):104008, 2018. ISSN 13616595. doi:[10.1088/1361-6595/aae5c3](https://doi.org/10.1088/1361-6595/aae5c3).
- [28] A Derzsi, T Lafleur, J.-P. Booth, A Derzsi, B Bruneau, and A R Gibson. Power coupling mode transitions induced by tailored voltage waveforms in capacitive oxygen discharges. *Plasma Sources Science and Technology*, 26:34002, 2017. doi:[10.1088/1361-6595/aa56d6](https://doi.org/10.1088/1361-6595/aa56d6).
- [29] A. Derzsi, T. Lafleur, J-P. Booth, and I. Korolov. Experimental and simulation study of a capacitively coupled oxygen discharge driven by tailored voltage waveforms. *Plasma Sources Science and Technology*, 25:015004, 2015. doi:[10.1088/0963-0252/25/1/015004](https://doi.org/10.1088/0963-0252/25/1/015004).
- [30] P. A. Delattre, T. Lafleur, E. Johnson, and J-P. Booth. Radio-frequency capacitively coupled plasmas excited by tailored voltage waveforms: Comparison of experiment and particle-in-cell simulations. *Journal of Physics D: Applied Physics*, 46(23):235201, 2013. ISSN 00223727. doi:[10.1088/0022-3727/46/23/235201](https://doi.org/10.1088/0022-3727/46/23/235201).
- [31] T. Lafleur, P. A. Delattre, E. V. Johnson, and J. P. Booth. Capacitively coupled radio-frequency plasmas excited by tailored voltage waveforms. *Plasma Physics and Controlled Fusion*, 55(12):124002, 2013. ISSN 07413335. doi:[10.1088/0741-3335/55/12/124002](https://doi.org/10.1088/0741-3335/55/12/124002).
- [32] S J Doyle, T Lafleur, A R Gibson, P Tian, M J Kushner, and J Dedrick. Enhanced control of the ionization rate in radio-frequency plasmas with structured electrodes via tailored voltage waveforms. *Plasma Sources Science and Technology*, 26:125005, 2017. doi:[10.1088/1361-6595/aa96e5](https://doi.org/10.1088/1361-6595/aa96e5).
- [33] I. Korolov, A. Derzi, Z. Donkó, E. Schüngel, and J. Schulze. The influence of electron reflection / sticking coefficients at the electrodes on plasma parameters in particle-in-cell simulations of capacitive radio-frequency plasmas. *Plasma Sources Science and Technology*, 25:15024, 2016. doi:[10.1088/0963-0252/25/1/015024](https://doi.org/10.1088/0963-0252/25/1/015024).
- [34] T Lafleur, P Chabert, and J.-P. Booth. Secondary electron induced asymmetry in capacitively coupled plasmas. *Journal of Physics D: Applied Physics*, 46(13):135201, 2013. ISSN 0022-3727. doi:[10.1088/0022-3727/46/13/135201](https://doi.org/10.1088/0022-3727/46/13/135201).
- [35] I Korolov, A Derzsi, and J Schulze. Asymmetry effect in capacitively coupled plasmas The influence of the secondary electron induced asymmetry on the electrical asymmetry effect in capacitively coupled plasmas. *Applied Physics Letters*, 064102(2013):1–5, 2014. doi:[10.1063/1.4817920](https://doi.org/10.1063/1.4817920).
- [36] S. Ries, L. Banko, M. Hans, D. Primetzhofer, J. M. Schneider, A. Ludwig, P. Awakowicz, and J. Schulze. Ion energy control via the electrical asymmetry effect to tune coating properties in reactive radio frequency sputtering. *Plasma Sources Science and Technology*, 28(11):114001, 2019. ISSN 1361-6595. doi:[10.1088/1361-6595/ab504b](https://doi.org/10.1088/1361-6595/ab504b).
- [37] S Brandt, B Berger, E Schüngel, I Korolov, A Derzsi, B Bruneau, E Johnson, T Lafleur, D O’Connell, M Koepke, T Gans, J P Booth, Z Donkó, and J Schulze. Electron power absorption dynamics in capacitive radio frequency

- discharges driven by tailored voltage waveforms in CF₄. *Plasma Sources Science and Technology*, 25(4):45015, 2016. ISSN 13616595. doi:[10.1088/0963-0252/25/4/045015](https://doi.org/10.1088/0963-0252/25/4/045015).
- [38] Y Zhang, A Zafar, D J Coumou, S C Shannon, and M J Kushner. Control of ion energy distributions using phase shifting in multi-frequency capacitively coupled plasmas. *Journal of Applied Physics*, 117(23):1–15, 2015. ISSN 10897550. doi:[10.1063/1.4922631](https://doi.org/10.1063/1.4922631).
- [39] Y Du and Y Li. Plasma Density Distribution in Asymmetric Geometry Capacitive Coupled Plasma Discharge System. *World Academy of Science, Engineering and Technology*, 6(11):919–922, 2012.
- [40] E Schüngel, J Schulze, Z Donkó, and U Czarnetzki. Power absorption in electrically asymmetric dual frequency capacitive radio frequency discharges. *Physics of Plasmas*, 18(1):13503, 2011. ISSN 1070664X. doi:[10.1063/1.3535542](https://doi.org/10.1063/1.3535542).
- [41] E Schüngel, D Eremin, J Schulze, T Mussenbrock, and U Czarnetzki. The electrical asymmetry effect in geometrically asymmetric capacitive radio frequency plasmas. *Journal of Applied Physics*, 112(5):53302, 2012. ISSN 00218979. doi:[10.1063/1.4747914](https://doi.org/10.1063/1.4747914).
- [42] D O’Connell, T Gans, E Semmler, and P Awakowicz. The role of the relative voltage and phase for frequency coupling in a dual-frequency capacitively coupled plasma. *Applied Physics Letters*, 93(8):2006–2009, 2008. ISSN 00036951. doi:[10.1063/1.2972117](https://doi.org/10.1063/1.2972117).
- [43] Z Donkó, J Schulze, B G Heil, and U Czarnetzki. PIC simulations of the separate control of ion flux and energy in CCRF discharges via the electrical asymmetry effect. *Journal of Physics D: Applied Physics*, 42(2):25205, 2009. ISSN 0022-3727. doi:[10.1088/0022-3727/42/2/025205](https://doi.org/10.1088/0022-3727/42/2/025205).
- [44] Edmund Schüngel, Robert Hofmann, Sebastian Mohr, Julian Schulze, Jürgen Röpcke, and Uwe Czarnetzki. Evaluation of the electrical asymmetry effect by spectroscopic measurements of capacitively coupled discharges and silicon thin film depositions. *Thin Solid Films*, 574:60–65, 2015. ISSN 00406090. doi:[10.1016/j.tsf.2014.11.059](https://doi.org/10.1016/j.tsf.2014.11.059).
- [45] B Bruneau, T Lafleur, T Gans, D O’Connell, A Greb, I Korolov, A Derzsi, Z Donkó, S Brandt, E Schüngel, J Schulze, P Diomede, D J Economou, S Longo, E Johnson, and J.-P. Booth. Effect of gas properties on the dynamics of the electrical slope asymmetry effect in capacitive plasmas: comparison of Ar, H₂ and CF₄. *Plasma Sources Science and Technology*, 25(1):01LT02, 2016. ISSN 0963-0252. doi:[10.1088/0963-0252/25/1/01LT02](https://doi.org/10.1088/0963-0252/25/1/01LT02).
- [46] I. Korolov, M. Leimkühler, M. Böke, Z. Donkó, V. Schulz-Von Der Gathen, L. Bischoff, G. Hübner, P. Hartmann, T. Gans, Y. Liu, T. Mussenbrock, and J. Schulze. Helium metastable species generation in atmospheric pressure RF plasma jets driven by tailored voltage waveforms in mixtures of He and N₂. *Journal of Physics D: Applied Physics*, 53(18):185201, 2020. ISSN 13616463. doi:[10.1088/1361-6463/ab6d97](https://doi.org/10.1088/1361-6463/ab6d97).
- [47] Y. Liu, F. J.J. Peeters, S. A. Starostin, M. C.M. Van De Sanden, and H. W. De Vries. Improving uniformity of atmospheric-pressure dielectric barrier discharges using dual frequency excitation. *Plasma Sources Science and Technology*, 27(1):01LT01, 2018. ISSN 13616595. doi:[10.1088/1361-6595/aaa568](https://doi.org/10.1088/1361-6595/aaa568).
- [48] S. Park, W. Choe, S. Y. Moon, and J. J. Shi. Electron Information in Single And Dual-Frequency Capacitive Discharges at Atmospheric Pressure. *Scientific Reports*, 8(1):7516, 2018. ISSN 20452322. doi:[10.1038/s41598-018-25892-w](https://doi.org/10.1038/s41598-018-25892-w).

- [49] D. Liu, A. Yang, X. Wang, C. Chen, M. Rong, and M. G. Kong. Electron heating and particle fluxes in dual frequency atmospheric-pressure helium capacitive discharge. *Journal of Physics D: Applied Physics*, 49(49):49LT01, 2016. ISSN 13616463. doi:[10.1088/0022-3727/49/49/49LT01](https://doi.org/10.1088/0022-3727/49/49/49LT01).
- [50] J. Waskoenig and T. Gans. Nonlinear frequency coupling in dual radio-frequency driven atmospheric pressure plasmas. *Applied Physics Letters*, 96(18):13–16, 2010. ISSN 00036951. doi:[10.1063/1.3425668](https://doi.org/10.1063/1.3425668).
- [51] S J Doyle, A R Gibson, R W Boswell, C Charles, and J P Dedrick. Control of electron, ion and neutral heating in a radio-frequency electrothermal microthruster via dual-frequency voltage waveforms. *Plasma Sources Science and Technology*, 28(3):35019, 2019. doi:[10.1088/1361-6595/ab0984](https://doi.org/10.1088/1361-6595/ab0984).
- [52] S Dixon, C Charles, R W Boswell, W Cox, J Holland, and R Gottscho. Interactions between arrayed hollow cathodes. *Journal of Physics D: Applied Physics*, 46(14):145204, 2013. ISSN 0022-3727. doi:[10.1088/0022-3727/46/14/145204](https://doi.org/10.1088/0022-3727/46/14/145204).
- [53] C. Charles, W. Liang, L. Raymond, J. Rivas-Davila, and R. W. Boswell. Vacuum Testing of a Miniaturized Switch Mode Amplifier Powering an Electrothermal Plasma Micro-Thruster. *Frontiers in Physics*, 5(August):1–8, 2017. ISSN 2296-424X. doi:[10.3389/fphy.2017.00036](https://doi.org/10.3389/fphy.2017.00036).
- [54] S Mazouffre. Electric propulsion for satellites and spacecraft: established technologies and novel approaches. *Plasma Sources Science and Technology*, 25(3):33002, 2016. ISSN 0963-0252. doi:[10.1088/0963-0252/25/3/033002](https://doi.org/10.1088/0963-0252/25/3/033002).
- [55] R A Arakoni, J J Ewing, and M J Kushner. Microdischarges for use as microthrusters: modelling and scaling. *Journal of Physics D: Applied Physics*, 41(10):105208, 2008. ISSN 0022-3727. doi:[10.1088/0022-3727/41/10/105208](https://doi.org/10.1088/0022-3727/41/10/105208).
- [56] C. Charles and R. W. Boswell. Measurement and modelling of a radiofrequency micro-thruster. *Plasma Sources Science and Technology*, 21(2):22002, 2012. ISSN 0963-0252. doi:[10.1088/0963-0252/21/2/022002](https://doi.org/10.1088/0963-0252/21/2/022002).
- [57] A Greig, C Charles, N Paulin, and R W Boswell. Volume and surface propellant heating in an electrothermal radio-frequency plasma micro-thruster. *Applied Physics Letters*, 105(5):54102, 2014. ISSN 0003-6951. doi:[10.1063/1.4892656](https://doi.org/10.1063/1.4892656).
- [58] T S Ho, C Charles, and R W Boswell. Performance modelling of plasma microthruster nozzles in vacuum. *Journal of Applied Physics*, 123(17):173301, 2018. ISSN 0021-8979. doi:[10.1063/1.5012765](https://doi.org/10.1063/1.5012765).
- [59] S J Doyle, A R Gibson, J Flatt, T S Ho, R W Boswell, C Charles, P Tian, M J Kushner, and J Dedrick. Spatio-temporal plasma heating mechanisms in a radio-frequency electrothermal microthruster. *Plasma Sources Science and Technology*, 27:85011, 2018. doi:[10.1088/1361-6595/aad79a](https://doi.org/10.1088/1361-6595/aad79a).
- [60] J Schulze, E Schüngel, Z Donkó, D Luggenhölscher, and U Czarnetzki. Phase resolved optical emission spectroscopy: a non-intrusive diagnostic to study electron dynamics in capacitive radio frequency discharges. *Journal of Physics D: Applied Physics*, 43(12):124016, 2010. ISSN 0022-3727. doi:[10.1088/0022-3727/43/12/124016](https://doi.org/10.1088/0022-3727/43/12/124016).
- [61] M J Kushner. Hybrid modelling of low temperature plasmas for fundamental investigations and equipment design. *Journal of Physics D: Applied Physics*, 42(19):194013, 2009. ISSN 0022-3727. doi:[10.1088/0022-3727/42/19/194013](https://doi.org/10.1088/0022-3727/42/19/194013).
- [62] A Salaba and R P Brinkmann. Non-neutral/quasi-neutral plasma edge definition for discharge models: A numerical example for dual frequency hydrogen capacitively coupled plasmas. *Japanese Journal of Applied Physics, Part 1: Regular Papers and Short Notes and Review Papers*, 45(6 A):5203–5206, 2006. ISSN 00214922. doi:[10.1143/JJAP.45.5203](https://doi.org/10.1143/JJAP.45.5203).

- [63] P Tian and M J Kushner. Controlling VUV photon fluxes in low-pressure inductively coupled plasmas. *Plasma Sources Science and Technology*, 24:34017, 2015. ISSN 0963-0252. doi:[10.1088/0963-0252/24/3/034017](https://doi.org/10.1088/0963-0252/24/3/034017).
- [64] M Hayashi. Report No. IPPJ-AM-19. Technical report, Nagoya Institute of Technology, 1991.
- [65] K Tachibana. Excitation of the 1s5, 1s4, 1s3 and 1s2 levels of argon by low-energy electrons. *Physical Review A*, 34(2):451, 1986. doi:[10.1103/PhysRevA.34.1007](https://doi.org/10.1103/PhysRevA.34.1007).
- [66] D Rapp and P EnglanderGolden. Total Cross Sections for Ionization and Attachment in Gases by Electron Impact. I. Positive Ionization. *The Journal of Chemical Physics*, 43(5):1464–1479, 1965. ISSN 0021-9606. doi:[10.1063/1.1696957](https://doi.org/10.1063/1.1696957).
- [67] N A Dyatko, Y Z Ionikh, I V Kochetov, D L Marinov, A V Meshchanov, A P Napartovich, F B Petrov, and S A Starostin. Experimental and theoretical study of the transition between diffuse and contracted. *J. Phys. D: Appl. Phys*, 41:55204, 2008. doi:[10.1088/0022-3727/41/5/055204](https://doi.org/10.1088/0022-3727/41/5/055204).
- [68] A Bogaerts, R G V Serikov, and V V Serikov. Calculation of gas heating in direct current argon glow discharges. *Journal of Applied Physics*, 87:8334, 1999. doi:[10.1063/1.373545](https://doi.org/10.1063/1.373545).
- [69] H W Ellis, R Y Pai, E W McDaniel, E A Mason, and L A Viehland. Transport Properties of Gaseous Ions Over a Wide Energy Range. *Atomic Data and Nuclear Data Tables*, 17(3):177–210, 1976. doi:[10.1016/0092-640X\(76\)90001-2](https://doi.org/10.1016/0092-640X(76)90001-2).
- [70] M A Furman and M T F Pivi. Probabilistic model for the simulation of secondary electron emission. *Physical Review Special Topics - Accelerators and Beams*, 5(12):82–99, 2002. ISSN 10984402. doi:[10.1103/PhysRevSTAB.5.124404](https://doi.org/10.1103/PhysRevSTAB.5.124404).
- [71] M A Lieberman. Analytical solution for capacitive RF sheath. *IEEE Transactions on Plasma Science*, 16(6):638–644, 1988. ISSN 00933813. doi:[10.1109/27.16552](https://doi.org/10.1109/27.16552).
- [72] A. Agarwal, S. Rauf, and K. Collins. Gas heating mechanisms in capacitively coupled plasmas. *Plasma Sources Science and Technology*, 21:55012, 2012. ISSN 0963-0252. doi:[10.1088/0963-0252/21/5/055012](https://doi.org/10.1088/0963-0252/21/5/055012).
- [73] C. Charles, R. Hawkins, and R. W. Boswell. Particle in cell simulation of a radiofrequency plasma jet expanding in vacuum. *Applied Physics Letters*, 106(9):93502, 2015. ISSN 0003-6951. doi:[10.1063/1.4914109](https://doi.org/10.1063/1.4914109).
- [74] T Lafleur and R W Boswell. Particle-in-cell simulations of hollow cathode enhanced capacitively coupled radio frequency discharges. *Physics of Plasmas*, 19(2), 2012. ISSN 1070664X. doi:[10.1063/1.3685709](https://doi.org/10.1063/1.3685709).
- [75] A. Derzsi, I. Korolov, E. Schüngel, Z. Donkó, and J. Schulze. Effects of fast atoms and energy-dependent secondary electron emission yields in PIC/MCC simulations of capacitively coupled plasmas. *Plasma Sources Science and Technology*, 24(3):34002, 2015. ISSN 13616595. doi:[10.1088/0963-0252/24/3/034002](https://doi.org/10.1088/0963-0252/24/3/034002).
- [76] T Gans, C C Lin, V Schulz-von der Gathen, and H F Döbele. Phase-resolved emission spectroscopy of a hydrogen rf discharge for the determination of quenching coefficients. *Phys. Rev. A*, 67:12707, 2003. ISSN 1050-2947. doi:[10.1103/PhysRevA.67.012707](https://doi.org/10.1103/PhysRevA.67.012707).
- [77] T Gans, D O’Connell, V Schulz-von der Gathen, and J Waskoenig. The challenge of revealing and tailoring the dynamics of radio-frequency plasmas. *Plasma Sources Science and Technology*, 19(3):34010, 2010. ISSN 0963-0252. doi:[10.1088/0963-0252/19/3/034010](https://doi.org/10.1088/0963-0252/19/3/034010).

- [78] S Siepa and U Czarnetzki. Line integration and spatial resolution in optical imaging of plasmas. *Journal of Physics D: Applied Physics*, 48:385201, 2015. doi:[10.1088/0022-3727/48/38/385201](https://doi.org/10.1088/0022-3727/48/38/385201).
- [79] J Schulze, Z Donkó, D Luggenhölscher, and U Czarnetzki. Different modes of electron heating in dual-frequency capacitively coupled radio frequency discharges. *Plasma Sources Science and Technology*, 18:34011, 2009. ISSN 0963-0252. doi:[10.1088/0963-0252/18/3/034011](https://doi.org/10.1088/0963-0252/18/3/034011).
- [80] W. Wiedermann and M. Hagmann. Asymmetric properties of the Pearson correlation coefficient: Correlation as the negative association between linear regression residuals. *Communications in Statistics - Theory and Methods*, 45(21):6263–6283, 2016. ISSN 1532415X. doi:[10.1080/03610926.2014.960582](https://doi.org/10.1080/03610926.2014.960582).
- [81] Y. Dodge and V. Rousson. On asymmetric properties of the correlation coefficient in the regression setting. *American Statistician*, 55(1):51–54, 2001. ISSN 00031305. doi:[10.1198/000313001300339932](https://doi.org/10.1198/000313001300339932).